

Fig. V.101. ($\text{U,Th})\text{Sb}$ s.c. (a) Hall resistivity, ρ_H , vs. temperature, T , for $x = 0.1$ at 6 and 9 T [82FSVA]. The solid lines are the high-temperature fits in the paramagnetic state to the equation: $\rho_H = \rho_{H0} + \rho_{HS} = B_i R_0 + 4\pi M R_S$, $B_i = H_i + 4\pi M$, R_0 yields about $N \approx 0.1\text{ e}^-/\text{f.u.}$ (see the Table in

Fig. V.100(a). (b) Normal R_0 and abnormal R_S Hall coefficients as a function of temperature in the ordered states (at $B = 6$ and 9 T the $x = 0.1$ composition behaves as a ferromagnet).

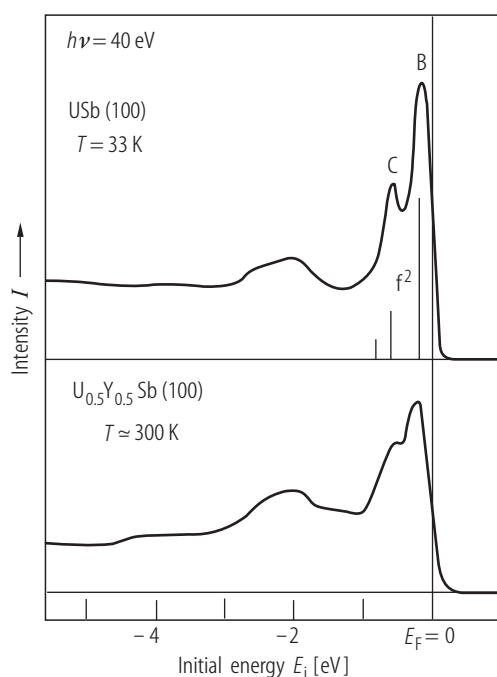


Fig. V.102. ($\text{U,Y})\text{Sb}$ s.c. Normalized (to equal 5p peak heights), angle integrated EDC's at $h\nu = 40\text{ eV}$ for $\text{U}_{0.5}\text{Y}_{0.5}\text{Sb}(100)$ taken at RT and compared to that in $\text{USB}(100)$ obtained at 33 K [82RMV]. The vertical bars for the USB -spectrum represent the f^2 final-state multiplet levels. Note partly suppressed 5f emission for the solid solution (peak B) however without a d-emission at E_F .

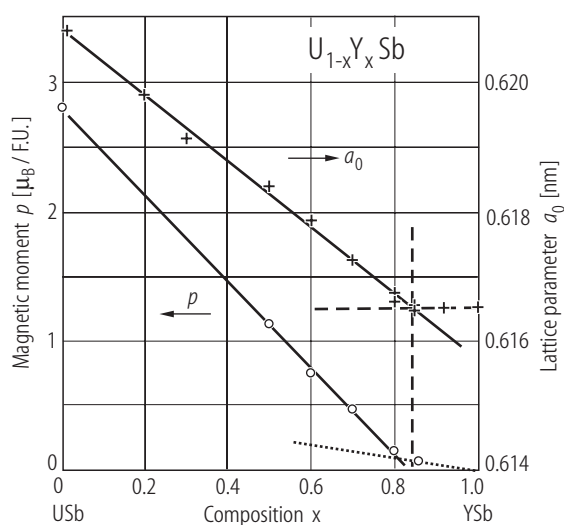


Fig. V.103. ($\text{U,Y})\text{Sb}$ s.c. Lattice parameter, a_0 , (rhs) and magnetic moment p (in $[\mu_B/\text{f.u.}]$) (lhs) as a function of Y – concentration x in the solid solutions $\text{U}_{1-x}\text{Y}_x\text{Sb}$ [84FSHV]. The values of p are taken from [82RBQV]. From the slope of straight lines p vs. x taken above and below $x \approx 0.82$ one derives $0.5\text{ } \mu_B/\text{Uat.}$ (dotted line) and $3.3\text{ } \mu_B/\text{U at.}$ (solid line) according to the assumption of a valence transition from U^{4+} into U^{3+} near $x \approx 0.85$ (dashed line, see the upper curve), respectively [84S3].

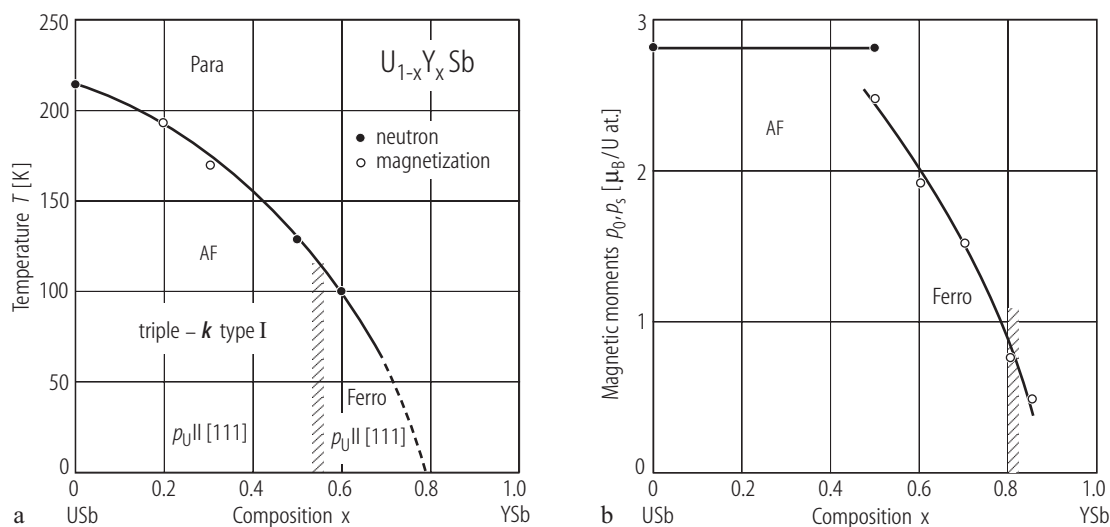


Fig. V.104. (U,Y)Sb. s.c. (a) (T , x) MPD of the solid solutions $\text{U}_{1-x}\text{Y}_x\text{Sb}$ [82RBQV]. Note that the Type AF I phase disappears for $x > 0.55$ and the ferromagnetic state occurs and that the ordering temperature decreases smoothly with x and reaches 0 K for $x \approx 0.8$ (compare with a similar

behaviour of the (U,Th)Sb, MPD (Fig. V.91). (b) Variation of the ordered magnetic moment p_0 (within AF I - $3k$) and p_s (determined at high field up to $B \sim 10$ T at $T = 4.2$ K) as a function of Y-doping x [82RBQV].

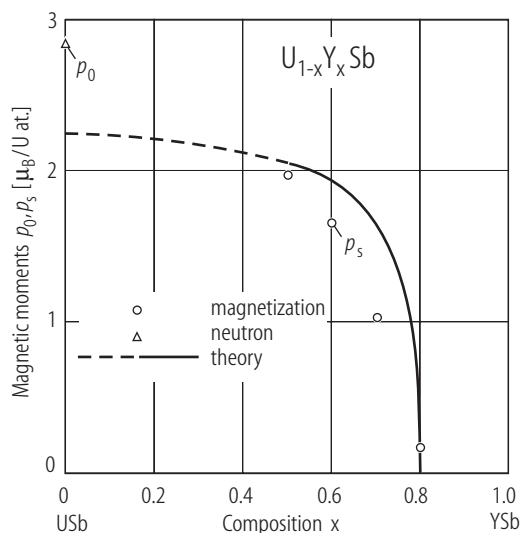


Fig. V.105. (U,Y)Sb. s.c. Ordered magnetic moments, p_0 (open triangle) and p_s (open circles), of the solid solutions $\text{U}_{1-x}\text{Y}_x\text{Sb}$ as a function of Y composition, x , [80CVS1]. The solid line presents a simple two-parameter model: i.e. containing $H_{\text{eff}} = H + \lambda M$ where $\lambda \equiv C_{\text{ex}}x$ and crystal-field splitting W (taking fourth-order terms only). The value C_{ex}/W is chosen to fit the critical concentration $x = 0.8$. $W = 24.2$ K and hence a crystal-field splitting to the first excited state $\Delta_{\text{CF}} = 339$ K. For possible valence change in this system see also [84FSHV] and Fig. V.103.

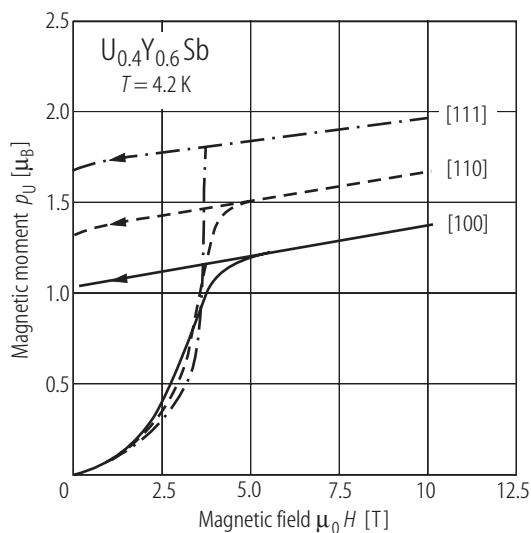


Fig. V.106. (U,Y)Sb. Magnetic moment per U atom, p_{U} , measured along the three main axes vs. applied magnetic field, H , up to 10 T for $\text{U}_{0.4}\text{Y}_{0.6}\text{Sb}$ at 4.2 K [80CVS1].

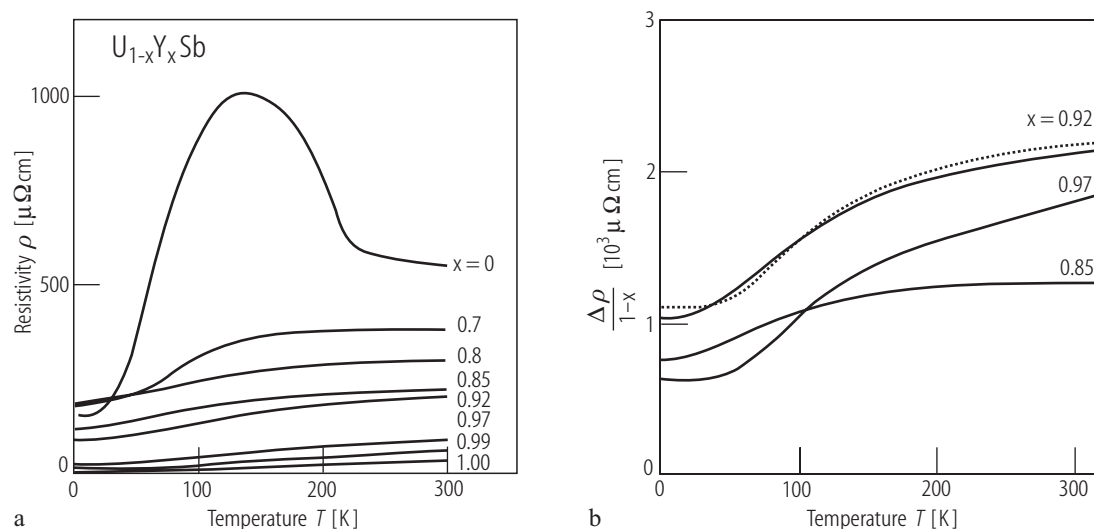


Fig. V.107. (U,Y)Sb s.c. (a) Electrical resistivity, ρ , of the solid solutions $\text{U}_{1-x}\text{Y}_x\text{Sb}$ with $x = 1, 0.99, 0.97, 0.92, 0.85, 0.80, 0.70, 0$, and (b) incremental electrical resistivity

$$\Delta\rho/(1-x) = \frac{\rho(\text{U}_{1-x}\text{Y}_x\text{Sb}) - \rho(\text{YSb})}{1-x} \quad \text{for samples with } x \leq 0.15 \text{ both as a function of temperature, } T, \text{ [84FSHV].}$$

The dotted line gives the theoretical electrical resistivity ρ_{th} vs. T for the case of two singlets separated by the energy of 265 K.

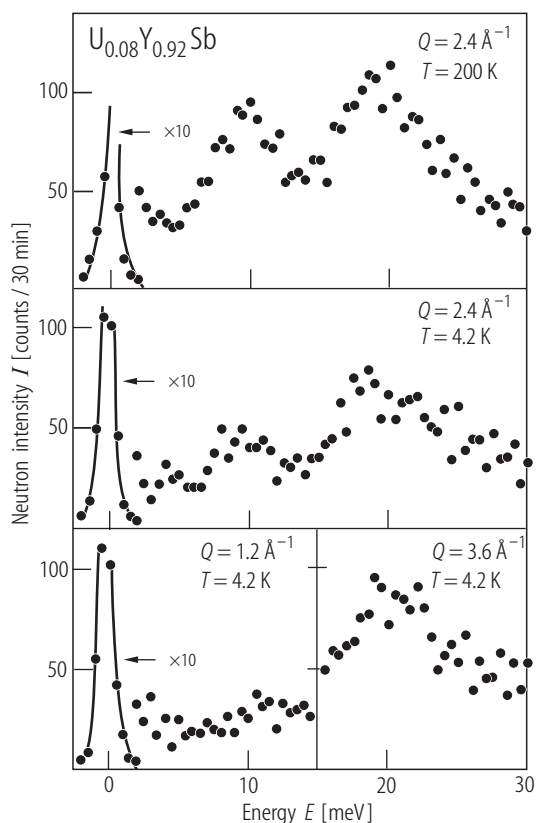


Fig. V.108. (U,Y)Sb. Inelastic neutron scattering spectra for polycrystalline solid solutions $\text{U}_{0.08}\text{Y}_{0.92}\text{Sb}$, representing a dilute 5f electron system in a so-called “cluster regime” [80FV]. The experiment was performed at various temperatures and momentum transfers in the energy range $0 \leq E \leq 55 \text{ meV}$. The broad lines centered at around 10 and 20 meV are probably due to phonon scattering while the high-energy shoulder of the 20 meV-peak is due to magnetic scattering, which can be interpreted as originating from crystal field splittings of the ground term of the U^{3+} ion according to the results of the form factor crystal-field analysis by [76LMSV].

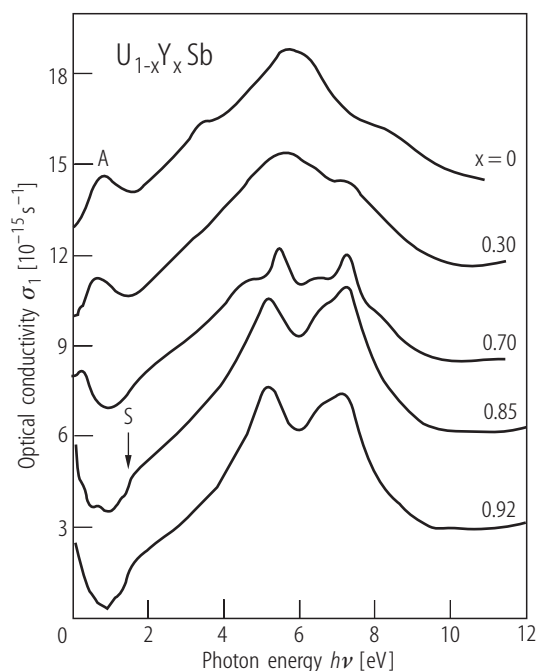


Fig. V.109. (U,Y)Sb s.c. Optical conductivity, σ_1 , vs. photon energy, $h\nu$, for the solid solutions $U_{1-x}Y_xSb$ with $x = 0, 0.30, 0.70, 0.85, 0.92$ [84S1]. For clarity, the consecutive curves are shifted by three units. Note a continuous shift of peak A (corresponding to $f \Rightarrow d$ transitions) to lower energies, on going from $x = 0.0$ to $x = 0.85$ where it finally disappears completely. This latter feature is assumed to be attributed to the promotion of one f electron into the conduction d -band (valence change) and then the remaining f^2 states for $x \geq 0.85$ give rise to $f^2 \Rightarrow d$ transitions (see a shoulder S near 1.6 eV). Thus, it allows deriving a Coulomb correlation energy of 1.5 – 2 eV [84FSHV]. The observed $f^3 \Rightarrow f^2$ valence transition at around $x \approx 0.85$ is correlated by the lattice parameter a_0 and magnetic moment variations with U- concentration x [82RBQV] (see Fig. V.103).

For Fig. V.110 see next page

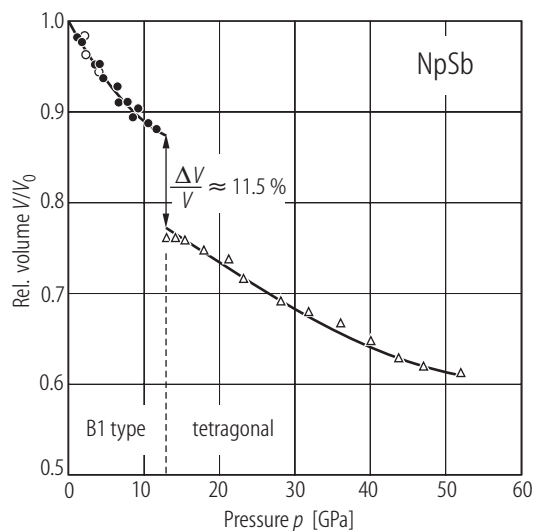


Fig. V.111. NpSb. Relative volume, V/V_0 , vs. pressure, p , up to 52 GPa [90DBHS]. $a_0 = 0.625117(5)$ nm. Closed circles: increasing pressure, open circles: decreasing pressure. At 13 GPa a first-order phase transition takes place (double-sided arrow) from the NaCl-type (B1) to a tetragonal (e.g. P4/mmm) structure being a distorted CsCl (B2)-type structure (open triangles). The bulk modulus B_0 and its pressure derivative B'_0 are given in Table 6. The occurrence at high pressure of the tetragonal phase instead of the CsCl-type one, usual for the monpnictides, is related to a covalent character of the Sb-Sb bonding and to the ratio of the cation to anion radii, which does not allow the CsCl-type structure to be formed.

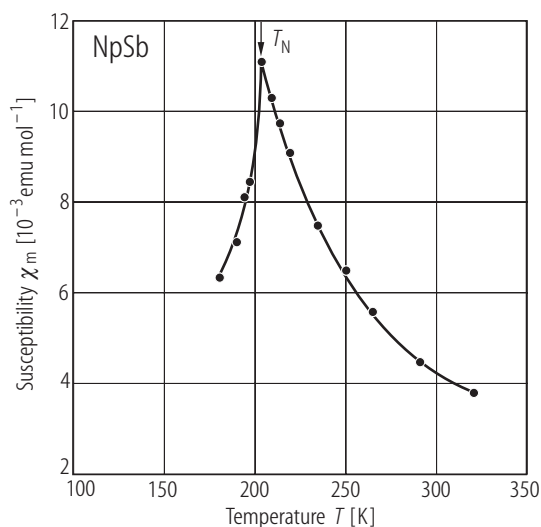


Fig. V.112. NpSb. Molar magnetic susceptibility, χ_m , vs. temperature, T , measured above 175 K (below this temperature the sample was impured by ferromagnetic Np_3Sb_4 compound) [72L]. $T_N = 205$ K, $p_{\text{eff}} = 2.3 \mu_B/\text{Np}$ found between 205...320 K.

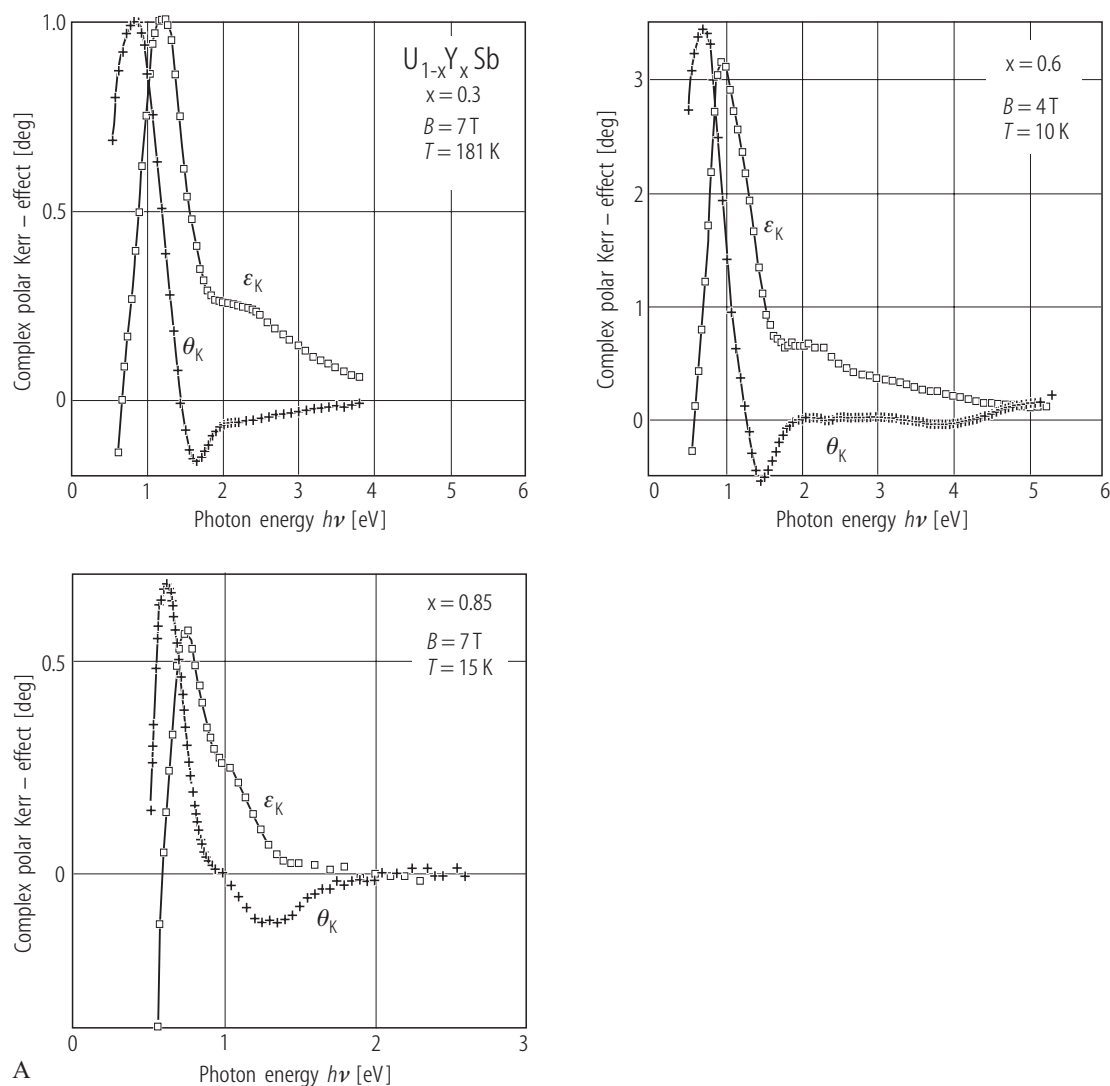


Fig. V.110. (U,Y)Sb s.c. **(A)** Complex polar Kerr-rotation, θ_K , and ellipticity, ϵ_K , of (100) cleaved single crystals of the $U_{1-x}Y_xSb$ solid solutions with $x = 0.3$ (AF), 0.6 (F) and 0.85 (Para) as a function of photon energy, $h\nu$, measured in applied magnetic fields and temperatures indicated [86R]. Note the different scales. See also that the $f \Rightarrow d$ transition (Figs III.50 and IV.70) feature narrows with dilution.

(B) Absorptive (σ_{2xy}) and dispersive (σ_{1xy}) part of off-diagonal conductivity for the three compositions indicated above (figure **(A)**). The dashed line ascribes σ_{xy} for $h\nu \leq 0.5$ eV obtained by Kramers-Kronig inversion [86R]. Note the different scales. See also a double structure for the $f \Rightarrow d$ transition well seen for $x = 0.85$.

For Fig. V.110B see next page

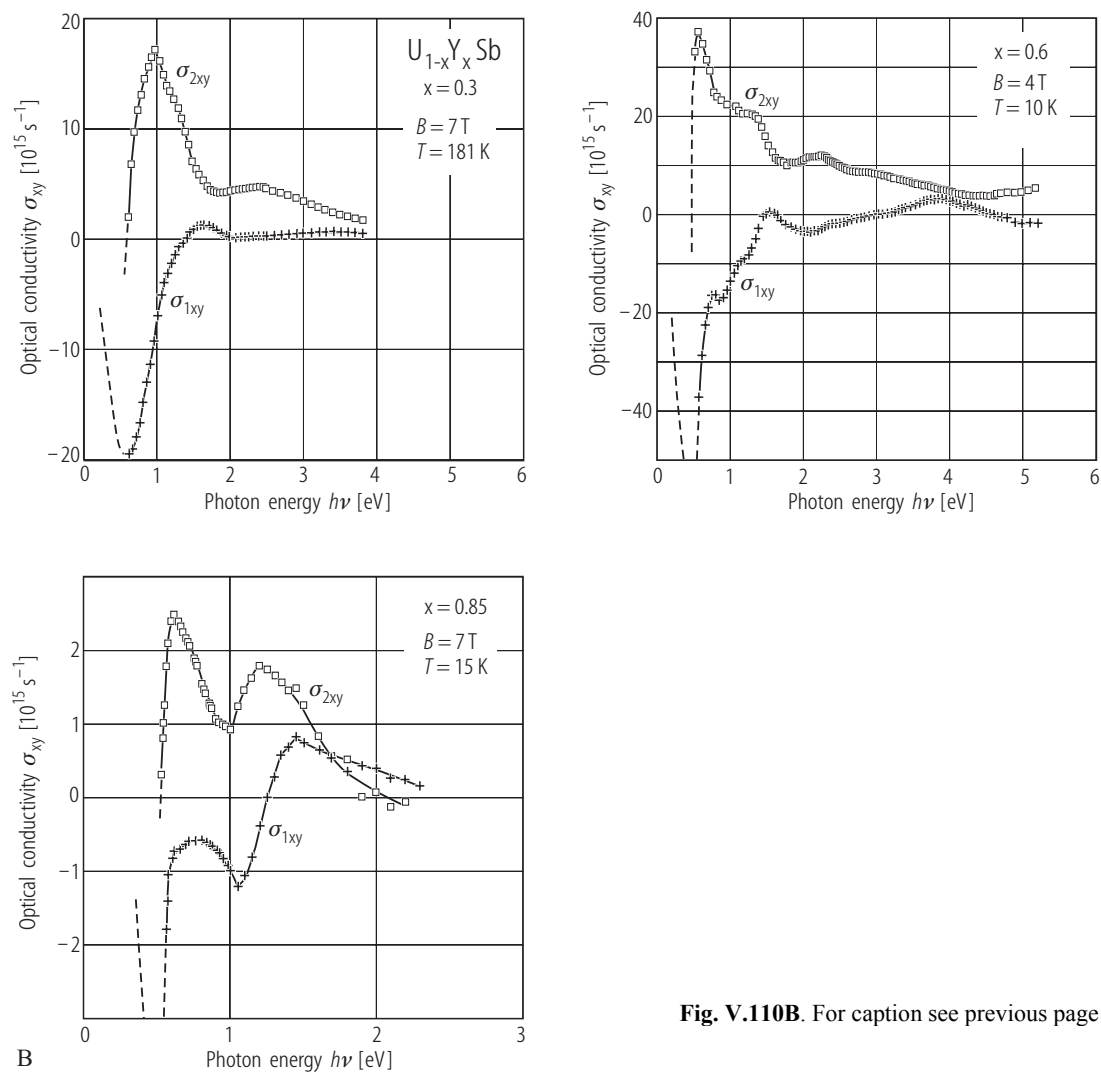


Fig. V.110B. For caption see previous page

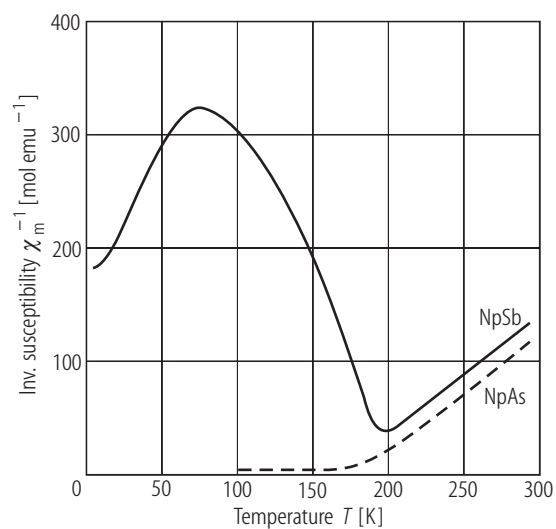


Fig. V.113. NpSb . s.c. Inverse molar susceptibility, χ_m^{-1} , vs. temperature, T , measured along [100] (solid line), compared to that of NpAs (dashed line) [89V], [92MVRs]. $T_N = 190 \text{ K}$, $\Theta_p = 161 \text{ K}$, $p_{\text{eff}} = 2.71 \mu_B$.

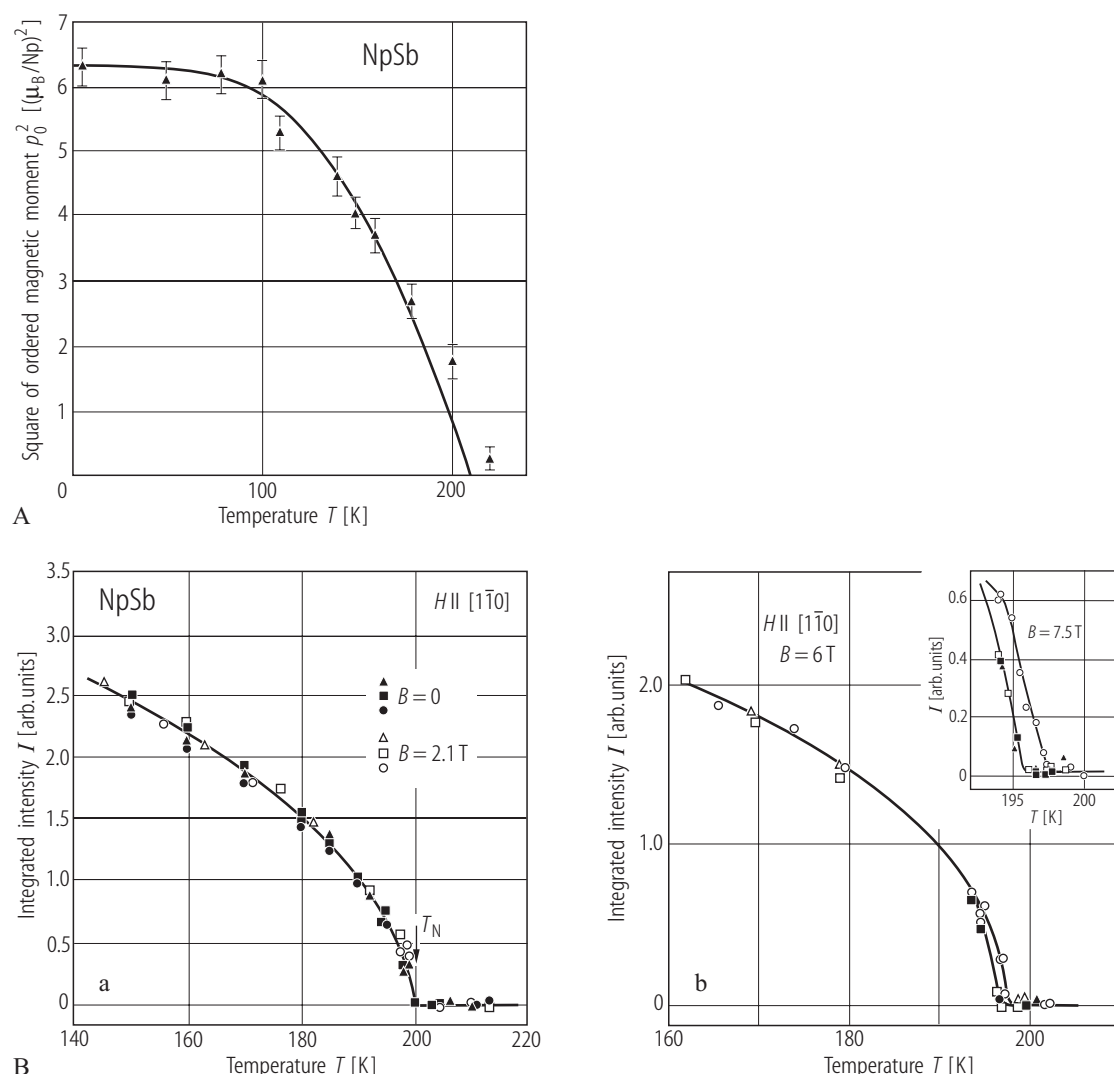


Fig. V.114. NpSb s.c. ND: **(A)** Square of the ordered moment, p_0^2 , vs. temperature, T , [74ADHL]. $p_0 = 2.51(7) \mu_B/\text{Np}$ measured on polycrystalline sample. The solid line represents the $(J_{1/2})^2$ function normalized to p_0 and T_N ($= 207$ K). (See LB III/12c, p.436, Fig. 71). **(B)** **(a)** Integrated intensity, I , vs. temperature, T , measured along the three \mathbf{k} -vectors: $[110]$ (circles), $[210]$ (squares) and $[120]$ (triangles) **(a)** at $B = 0$ (full symbols) and $B = 2.1$ T (open symbols) and **(b)** at 6 T [88SBQB]. For the former field the intensities $I(\mathbf{k}_1)$, $I(\mathbf{k}_2)$, $I(\mathbf{k}_3)$, associated with the three \mathbf{k} -vectors, $\mathbf{k}_1 =$

$[100]$, $\mathbf{k}_2 = [010]$, and $\mathbf{k}_3 = [001]$ are like those in zero-field, which rules out the domain motion upon cooling through T_N . This proves a triple- \mathbf{k} structure. For the latter case the intensity $I(\mathbf{k}_3)$ with $\mathbf{k}_3 \perp B$ at temperatures close to T_N has a non-zero intensity which is a result of breaking the triple- \mathbf{k} structure which in turn induces a collinear ordering. On further cooling the intensities $I(\mathbf{k}_1)$ and $I(\mathbf{k}_2)$ increase up to the recovering of the triple- \mathbf{k} one. In the inset this situation is shown for $B = 7.5$ T. $p_0 = 2.50(5) \mu_B$.

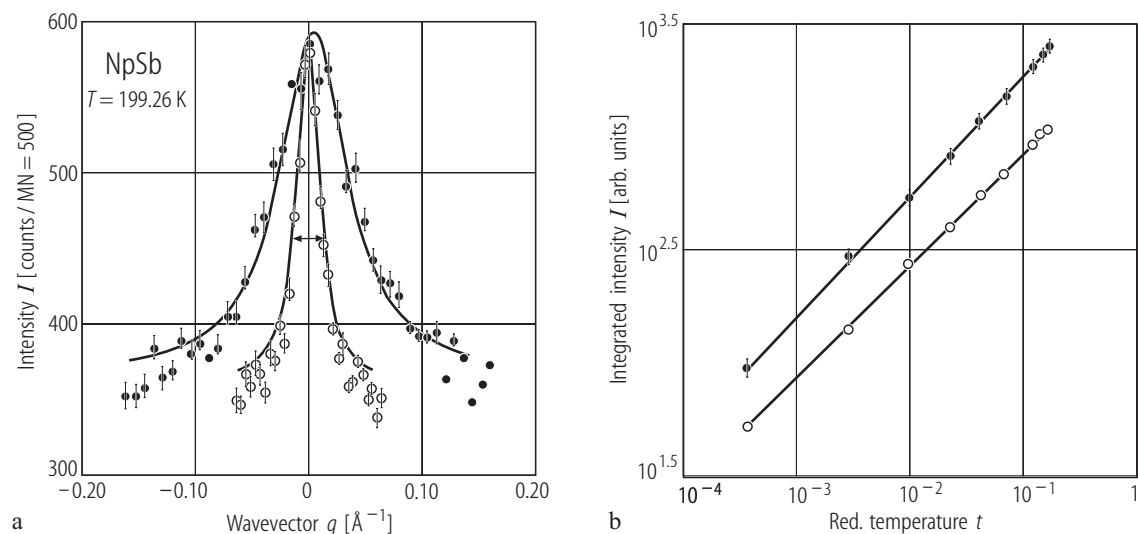


Fig. V.115. NpSb s.c. **(a)** Critical scattering. Monitored neutron scans showing the anisotropy in the critical scattering. Measurements were carried out at $T = 199.26$ K ($t = 1.3 \cdot 10^{-3}$) along two directions: 1) (00η) (closed circles) and 2) $(\eta\eta0)$ (open circles) [91JSLR]. A similar behaviour was found for NpAs [91JSLR], see Fig. IV.104. **(b)** A double log plot of integrated intensity, I , vs. reduced temperature, t , for the (110) magnetic Bragg peak, measured

below T_N [91JSLR]. $p_{Np} = 2.5(1) \mu_B$. The two straight lines correspond to least-squares fit to the experimental points taken with (open circles) and without (solid circles) an analyzer, respectively. From the fit $T_N = 199.01(2)$ K and the mean value of $\beta = 0.257(5)$ were derived. The anisotropy correlation ratio $R = 4.5(1)$ is high and similar to that for USb ($5.0(5)$), both having the type I- $3k$ magnetic structure, see Fig. IV.106

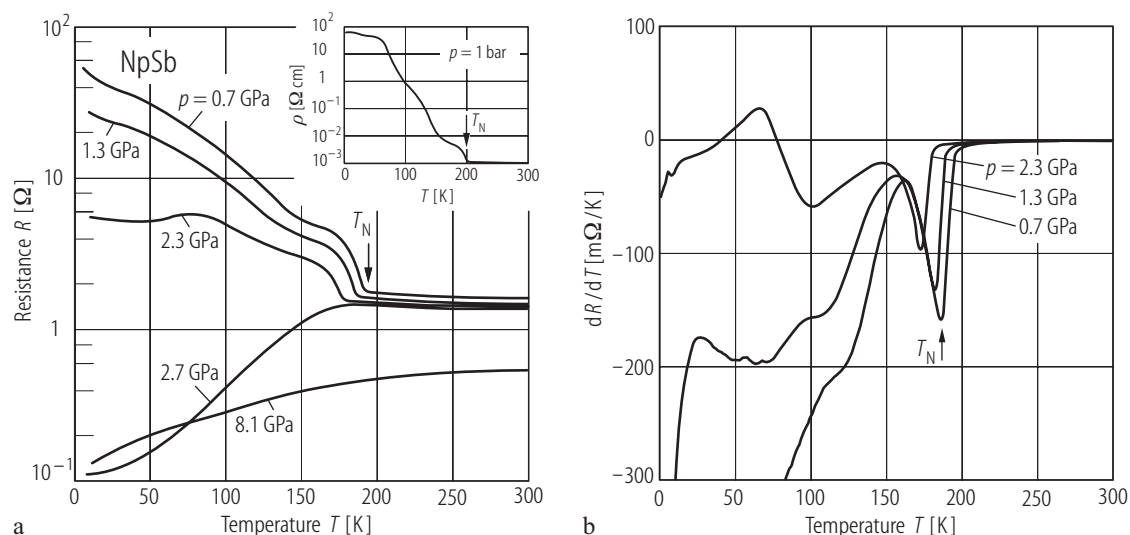


Fig. V.116. NpSb s.c. **(a)** Electrical resistance R vs. temperature, T , at pressures, p , up to 8.1 GPa taken from [94ABIB] and presented in [97IZBS]. $T_N \approx 200$ K. The inset shows the electrical resistivity, ρ , vs. temperature, T , at ambient pressure. Note a semiconductor like behaviour

below T_N and that T_N decreases with increasing pressure. Note also the sudden change in the $R(T)$ behaviour above 2.3 GPa. **(b)** The derivative dR/dT vs. temperature, T , [94ABIB]. T_N appears as a sharp negative peak. $dT_N/dp = -11.5$ K/GPa.

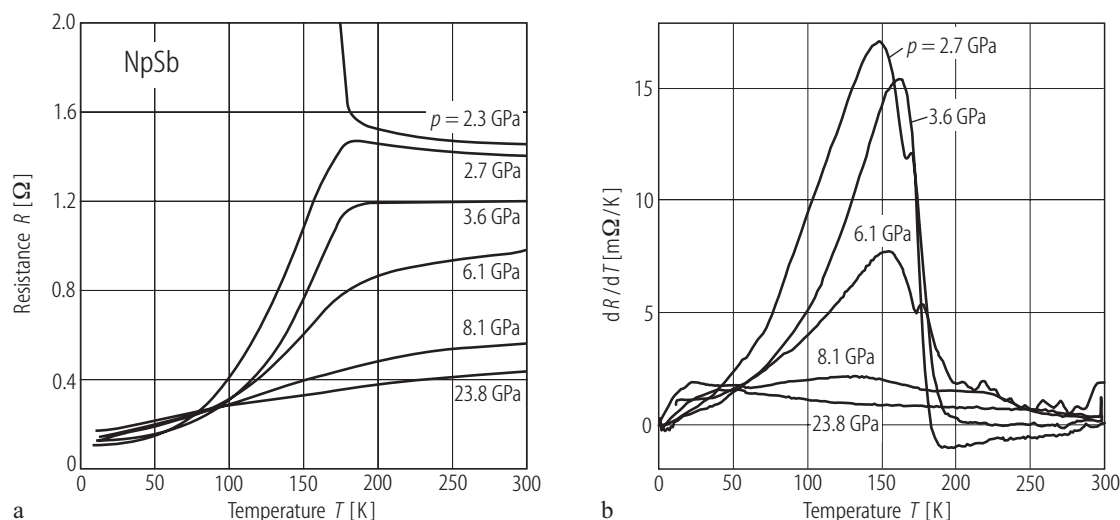


Fig. V.117. NpSb s.c. (a) Electrical resistance, R , vs. temperature, T , at pressures from 2.3 to 23.8 GPa [94ABIB]. Note the dramatic change of the behaviour under higher pressure than 2.3 GPa. At higher temperatures above T_N the Kondo-like resistivity changes to typical

metallic behaviour. (b) The derivative dR/dT vs. temperature, T , [94ABIB]. Note a double discontinuity in the resistance, appearing as a double peak in its temperature derivative.

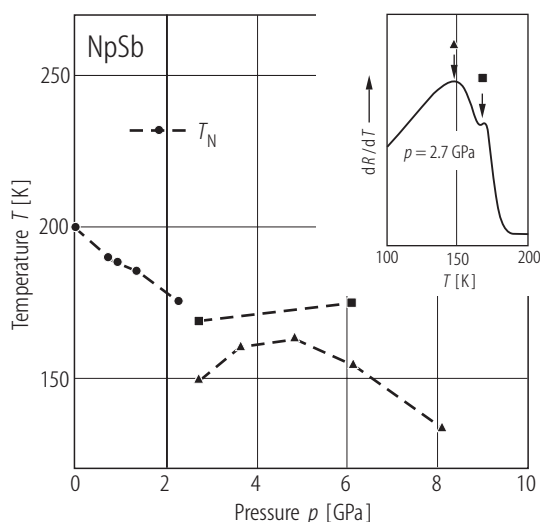


Fig. V.118. NpSb s.c. The Néel temperature, T_N , and other characteristic temperatures (explained in the inset), as a function of pressure, p , [94ABIB]. $dT_N/dp = -11.5$ K/GPa and $d\ln T_N/d\ln V = 3.1$.

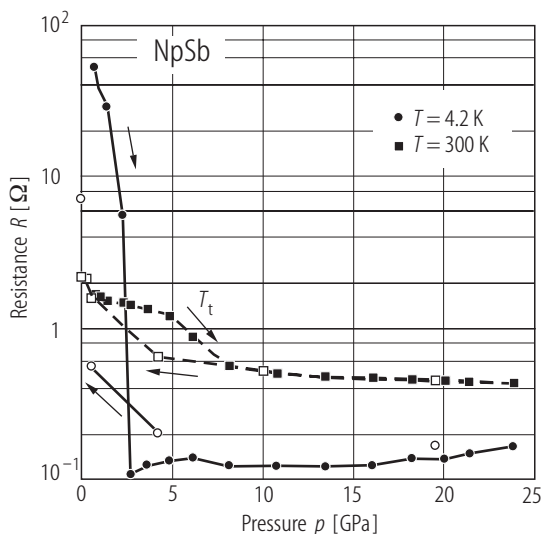


Fig. V.119. NpSb s.c. Electrical resistance R vs. pressure, p , measured at constant temperatures 4.2 and 300 K [94ABIB]. Solid and open symbols correspond to increasing and releasing pressure, respectively. The change in R at RT, occurring between 5...8 GPa, is probably connected with the change of crystal structure, despite the large difference in transition pressures (10...18 GPa) found from X-ray (see [88SBQB]), while the dramatic change observed at 4.2 K below 3 GPa is probably of not structural origin.

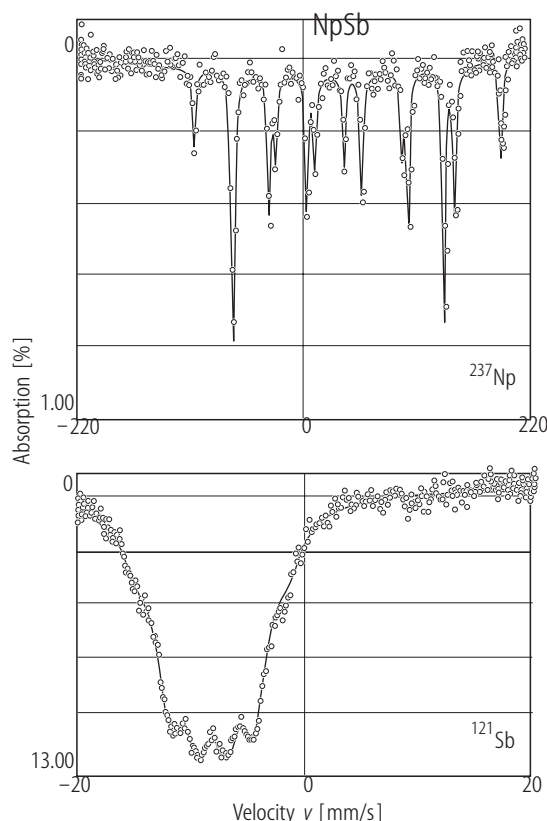


Fig. V.120. NpSb. Mössbauer spectra at 4.2 K for ^{237}Np (top) and ^{121}Sb (bottom) [88SBQB]. The magnetic moments order antiferromagnetically below $T_N = 200$ K in a type I- $3k$ magnetic structure. The U and Np mononictides exhibit large similarities characterized by an increase of T_0 when increasing the weight of the anion and of the stability of the multi- k order. From the known equation ($B_{\text{hf}}/p_0 = 215 \text{ T}/\mu_B$) p_0 at 4.2 K is $2.56(10) \mu_B/\text{Np}$ atom with good agreement with the neutron value. Compare these data with those for NpN and NpP [74ADHL] as well as for NpAs [87PMPL]. The hyperfine field B_{hf} and the quadrupole coupling constant (see the Table) are close to the values of free ion Np^{3+} ($B_{\text{hf}} = 530 \text{ T}$, $e^2qQ = -27.3 \text{ mm/s}$, i.e. $eq(1-R) = -1.32 \cdot 10^{18} \text{ V/cm}^2$ [85DK]). From ^{121}Sb results a strong mixing of 5f electrons with the anion p states has been concluded.

Table: ^{237}Np and ^{121}Sb hyperfine parameters.

	B_{hf}	e^2qQ	IS	Γ
	[T]	[mm/s]	[mm/s]	[mm/s]
^{237}Np	550	-25.8	21.6(2) ^{a)}	3.4(3)
^{121}Sb	16.4	0	-8.24(5) ^{b)}	2.85(1)

Isomer shifts relative to: ^{a)} NpAl_2 and ^{b)} LaSnO_3 sources.

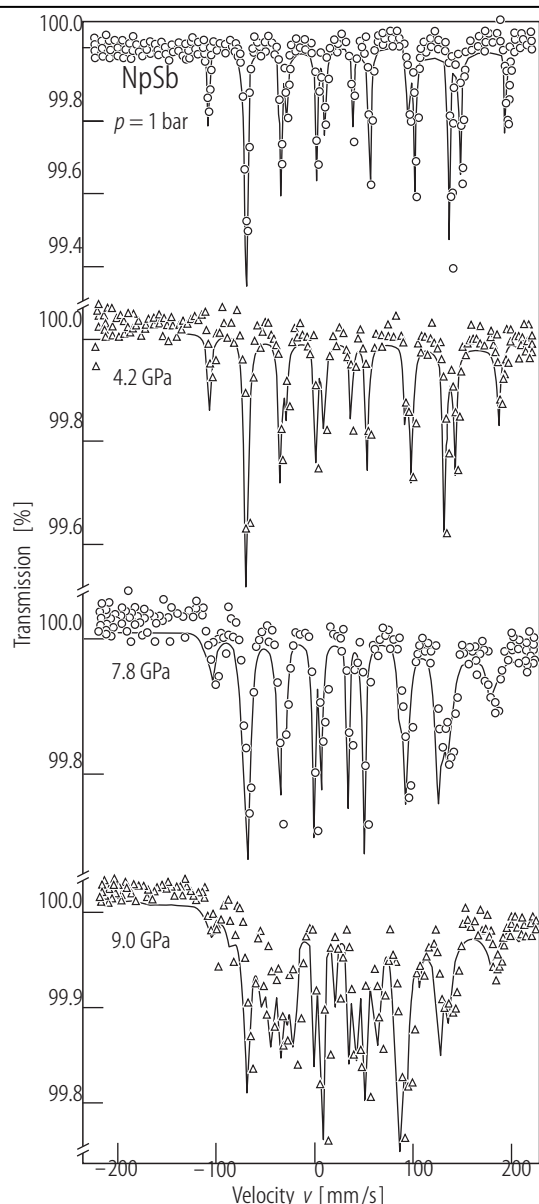


Fig. V.121. NpSb. Mössbauer spectra recorded at 4.2 K under pressures up to 9.0 GPa [97IZBS]. At 7.8 GPa an additional line broadening takes place probably due to a change of the spin arrangement and at 9.0 GPa, the spectrum is fitted by two subspectra, which correspond to two different sites of Np atoms (see Fig. V.122). The relative intensities of the two subspectra 1 and 2 are close to 1:1. See also the work by [88SBQB].

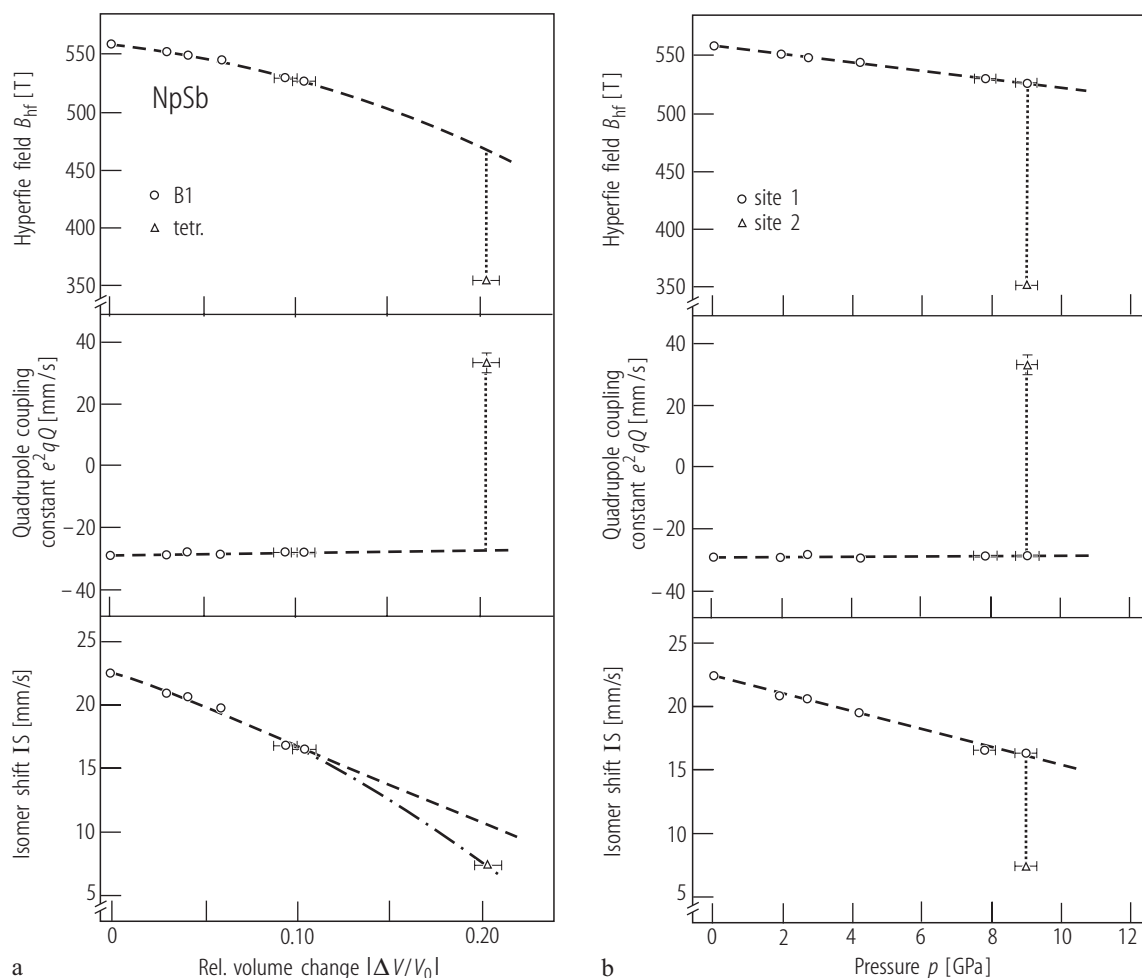


Fig. V.122. NpSb. **(a)** Hyperfine field, B_{hf} , quadrupole interaction, e^2qQ , and the isomer shift, IS, (relative to $NpAl_2$) as a function of volume change $\Delta V/V_0$ [97IZBS]. Note that at higher pressures two crystallographic phases can be identified, the NaCl phase (open circle) and the tetragonal phase (open triangles). The relative intensities IS_1 and IS_2 ($\sim 50\%$) of the subspectra of sites 1 and 2 point to about the same weight of these two phases. At site 2, B_{hf2} is drastically reduced by more than 30%, the quadrupole

coupling constant $(e^2qQ)_2$ has opposite sign, and isomer shift IS_2 is reduced by ~ 9 mm/s relative to IS_1 . **(b)** Hyperfine field B_{hf} , quadrupole interaction e^2qQ and the isomer shift IS (relative to $NpAl_2$) as a function of pressure, p [97IZBS], [98BDGI]. At higher pressures two Np sites can be distinguished. At site 2, B_{hf2} is drastically reduced by more than 30%, the quadrupole coupling constant $(e^2qQ)_2$ has opposite sign, and isomer shift IS_2 is reduced by ~ 9 mm/s relative to IS_1 .

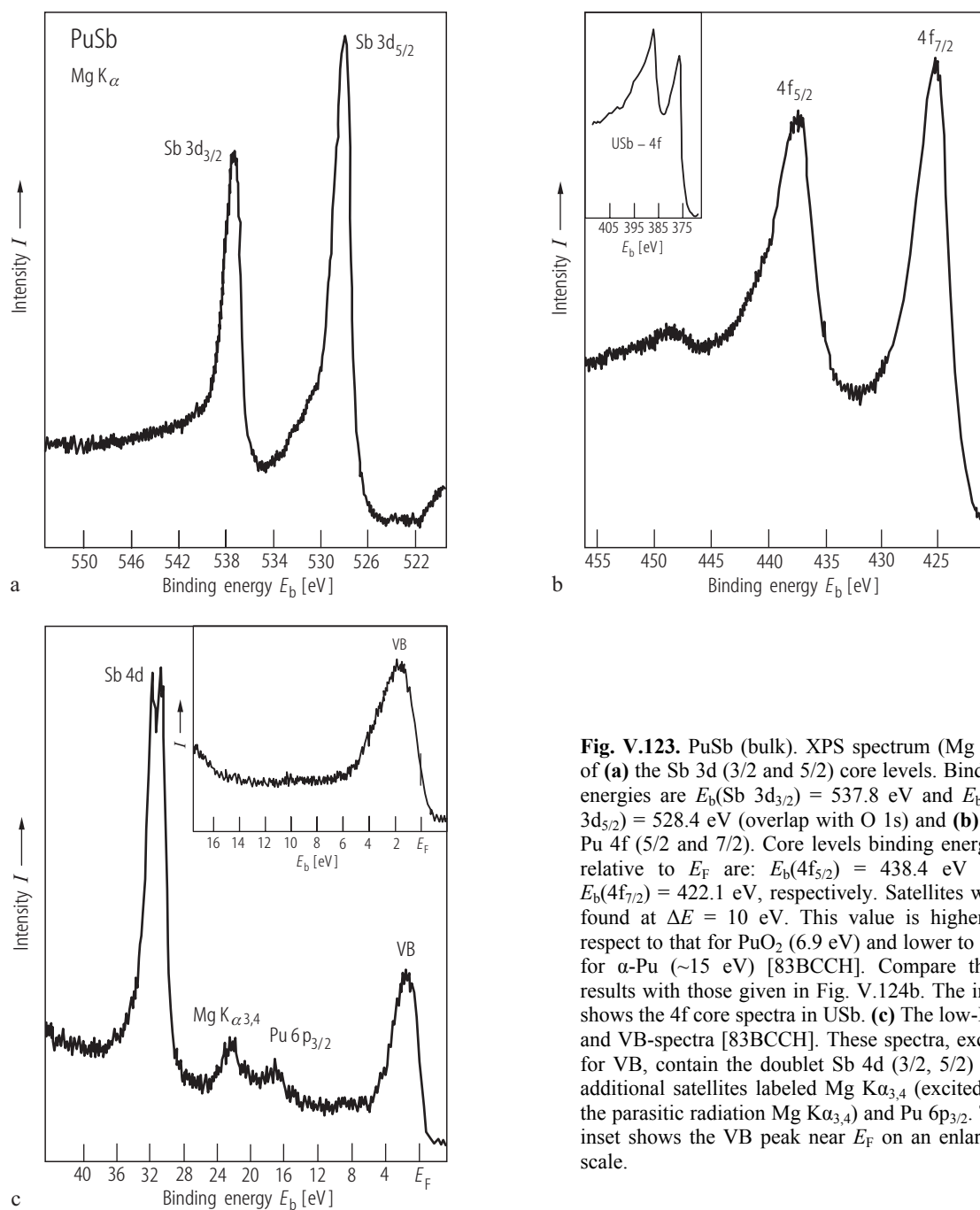


Fig. V.123. PuSb (bulk). XPS spectrum (Mg K α) of (a) the Sb 3d (3/2 and 5/2) core levels. Binding energies are $E_b(\text{Sb } 3d_{3/2}) = 537.8$ eV and $E_b(\text{Sb } 3d_{5/2}) = 528.4$ eV (overlap with O 1s) and (b) the Pu 4f (5/2 and 7/2). Core levels binding energies relative to E_F are: $E_b(4f_{5/2}) = 438.4$ eV and $E_b(4f_{7/2}) = 422.1$ eV, respectively. Satellites were found at $\Delta E = 10$ eV. This value is higher in respect to that for PuO $_2$ (6.9 eV) and lower to that for α -Pu (~ 15 eV) [83BCCH]. Compare these results with those given in Fig. V.124b. The inset shows the 4f core spectra in USb. (c) The low-BE- and VB-spectra [83BCCH]. These spectra, except for VB, contain the doublet Sb 4d (3/2, 5/2) and additional satellites labeled Mg K $\alpha_{3,4}$ (excited by the parasitic radiation Mg K $\alpha_{3,4}$) and Pu 6p $_{3/2}$. The inset shows the VB peak near E_F on an enlarged scale.

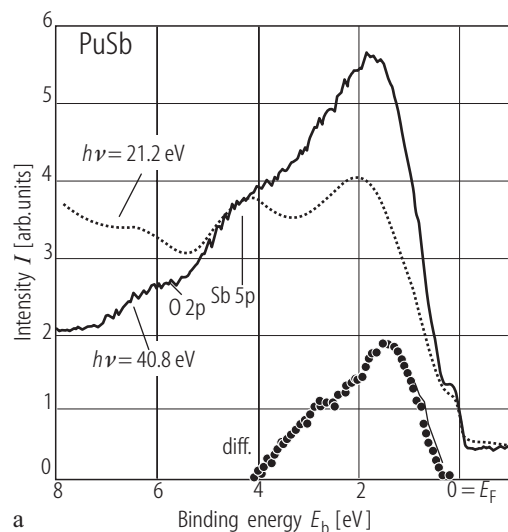


Fig. V.124. PuSb (thin layers). **(a)** UPS valence band spectra [00GWRH]. The solid and dotted lines represent the spectra with $h\nu = 40.8$ (HeII) and 21.2 eV (HeI). The solid circles show the difference spectrum. As seen, the HeII spectrum displays a maximum at 1.8 eV, a shoulder at 4 eV (Sb $5p$) and a small hump at 6 eV (O $2p$), respectively. After renormalization of the spectra, it is concluded that the $5f$ states *do not contribute* to the emission at E_F . Hence the 2 eV maximum corresponds to a multiplet of localized $5f'$ states. The strongly reduced intensity at E_F is attributed, at least partially, to Pu $6d$ states. **(b)** The background subtracted $4f$ -core level spectra of PuSb compared to those of bulk α -Pu [00GWRH]. If for α -Pu there are observed both peaks, namely the asymmetric well screened $4f_{7/2}$ main peak and almost symmetric, poorly screened peak located about 3 eV higher in BE and having a small spectra weight, then for PuSb there is observed only the latter one, reflecting unambiguously the $5f$ electron localization [00GWRH].

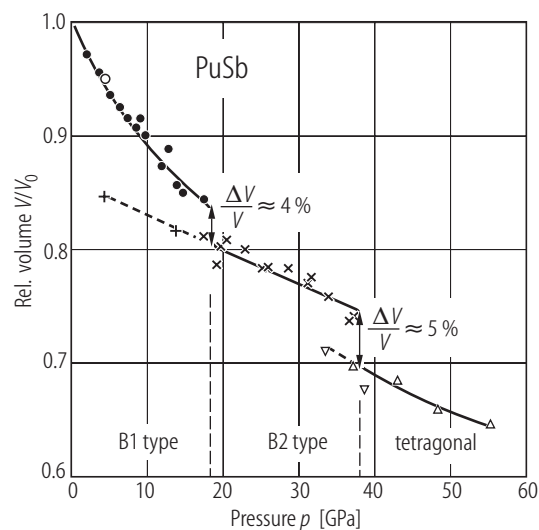
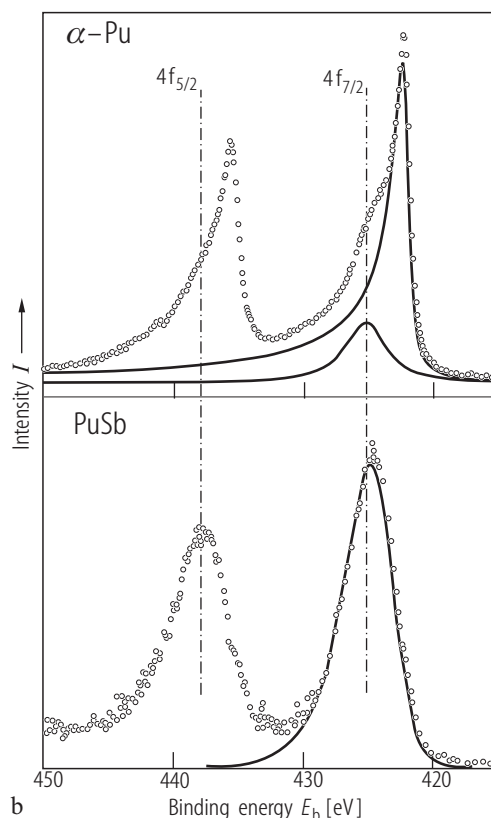


Fig. V.125. PuSb. Relative volume, V/V_0 , vs. pressure, p , up to 57 GPa [89BDDL], [90DBHS]. $a_0 = 0.62375(5)$ nm. B1-type: increasing pressure (closed circle), decreasing pressure (open circles). At 17 GPa and 38 GPa two phase transitions take place first into B2-type structure (crosses) and then into a tetragonal one with s.g. $P4/mmm$ (open triangles). The latter structure is of distorted CsCl-type and analogous to that in NpSb [92BDHD], see Fig. V.111. In case of releasing pressure a hysteresis down to 33 GPa from the tetragonal to B2-type phase transition is observed. The latter in turn was maintained down to 4 GPa, where the B1 structure was recovered. The first transition is typical for NaCl-type actinide compounds and does not involve $5f$ electrons, but is mainly governed by the $7s6d$ electrons. The second transition is related to strong p-f mixing effect occurring in PuSb and results in some delocalization of the $5f$ electrons. The bulk modulus, B_0 , and its pressure derivative, B_0' are given in Table 6.

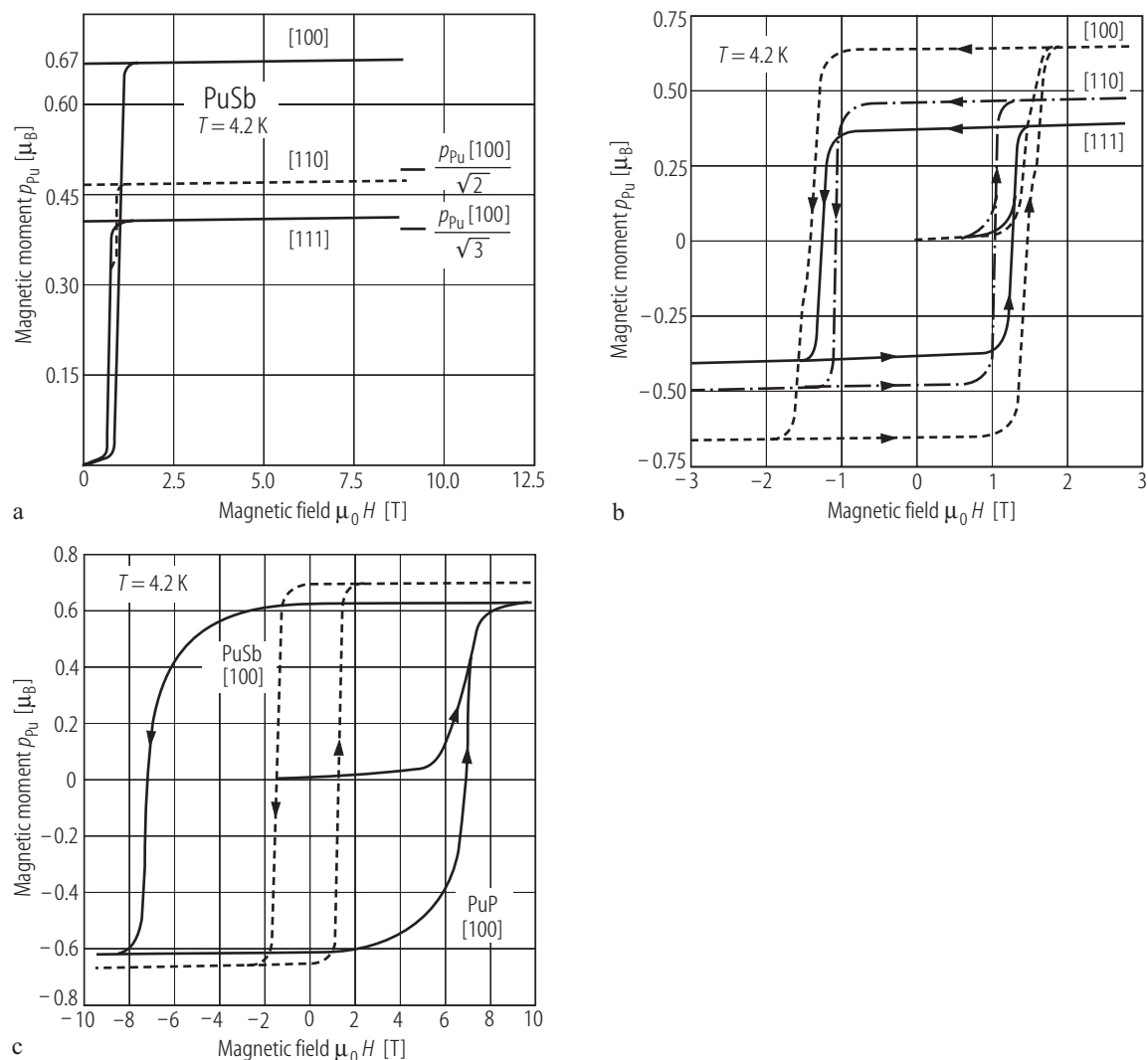


Fig. V.126. PuSb s.c. (a) Magnetic moment per Pu atom, p_{Pu} , vs. applied magnetic field, H , at 4.2 K [83CTSM]. $T_C = 75$ K, $T_N = 85$ K. The magnetization is extremely anisotropic, with the magnetization easy axis along the [100] direction. The horizontal bars mark values of projection of the moment onto the [110] and [111] direction. $p_s = 0.67 \mu_B/\text{Pu at}$. (b) Hysteresis loops measured at 4.2 K

along three axes [100], [110] and [111], as a function of applied field H up to 3 T (presented in [86F]). (c) Hysteresis loops of PuSb compared to that in PuP. Both taken along the [100] axis at 4.2 K [92MV]. This gives evidence for the difference in magnetocrystalline anisotropy between these two mononictides. In the case of PuP a field as large as 6 T is required to move the Bloch walls.

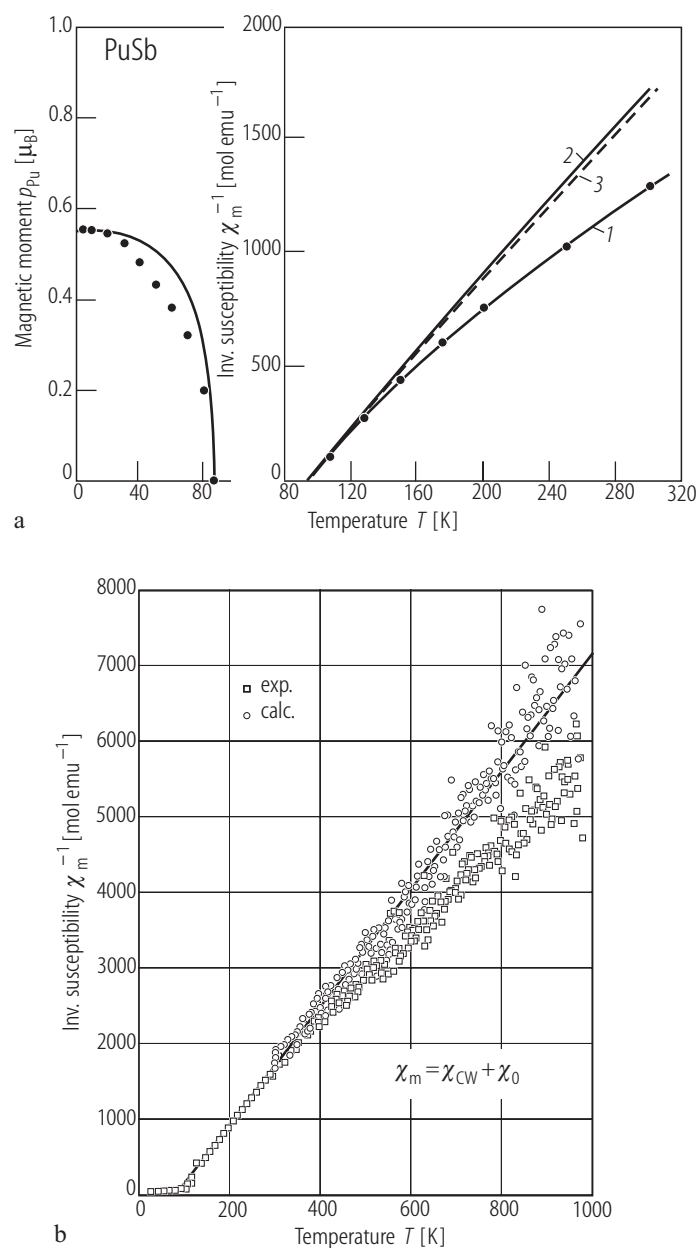


Fig. V.127. PuSb poly and s.c. **(a)** Polycrystal: Right: Inverse molar magnetic susceptibility, χ_m^{-1} , vs. T up to 300 K [72L]. Measured (closed symbols) and calculated (solid and dashed lines) quantities. Left: Magnetic moment as a function of temperature. Calculations were done using a nonperturbative treatment of crystalline electrical fields (intermediate coupling scheme) [70CL]. $A_4\langle r^4 \rangle = 2365 \text{ cm}^{-1}$, $A_6\langle r^6 \rangle = 750 \text{ cm}^{-1}$, molecular field $\mu_0 H_m = 900 \text{ T}$. Curve 1) measured:

temperature dependent χ_m^{-1} (solid points and line), curve 2): $(\chi_m - \chi_0)^{-1}$ vs. T (solid line), curve 3): calculated $\chi_{\text{Pu}^{3+}}^{-1}$ vs. T dependence (dashed line). $\chi_0 = 0.2 \cdot 10^{-3} \text{ emu/mol}$, $p_{\text{eff}} = 1.0 \mu_B$, $p_s = 0.57 \mu_B/\text{Pu at.}$, $T_C = 85(5) \text{ K}$. **(b)** s.c.: χ_m^{-1} vs. T up to 1000 K [98VMLR]. The scattering of the point is due to a small signal of the sample itself as well as due to the large contribution of the encapsulation. The parameters of a MCW law are $\chi_0 = 40 \cdot 10^{-6} \text{ emu/mol}$, $\Theta_p = 85 \text{ K}$, $p_{\text{eff}} = 1.0 \mu_B$.

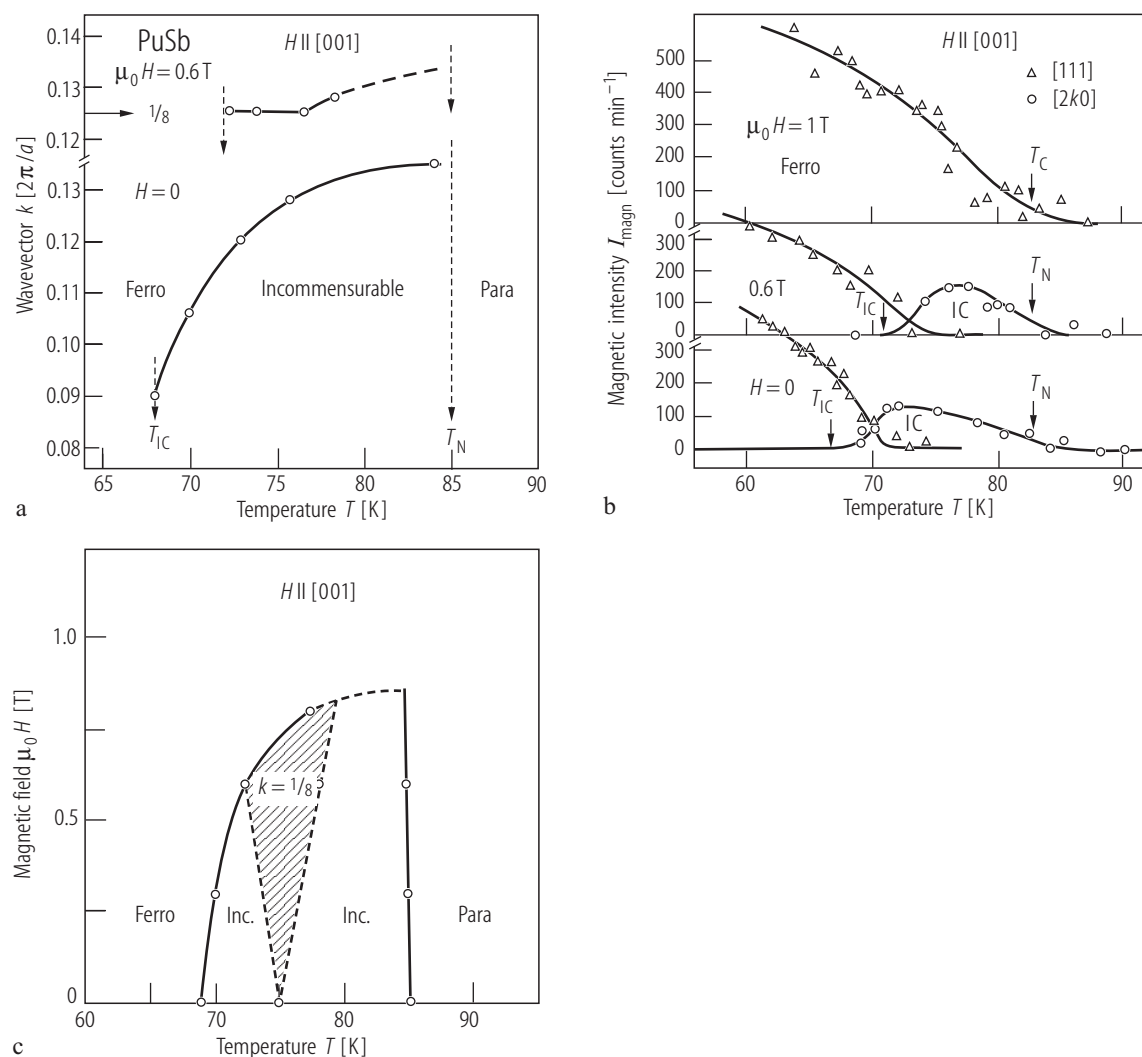


Fig. V.128. PuSb s.c. **(a)** The incommensurate wave vector k vs. temperature, T , at $H = 0$ (lower curve) and at $\mu_0 H = 0.6$ T (upper curve) applied along [001] [84BQRS]. $k \parallel m_k$ and its value varies from $k = 0.135(5)$ at T_N ($= 85$ K) to $k = 0.090(5)$ at T_C ($\equiv T_{IC} = 67$ K). The difference (at $H = 0$) $k(T_N) - k(T) = a(T_N - T)^3$ with $a = 1.25 \cdot 10^{-3}$ rlu/K³ (solid line). The magnetic field along the [001] axis modifies the IC phase, k locks into commensurate value of $1/8$. **(b)** Neutron magnetic intensity, I_{magn} , vs. temperature, T , in different applied magnetic field, H (indicated) [84BQRS]. Note that the applied field does not affect the ordering transition ($T_N = 85(1)$ K), whereas the IC-transition ($T_{IC} = 67$ K, $H = 0$) is

strongly shifted to higher temperatures. A high magnetic field such as 0.85 T is enough to suppress the incommensurate state. **(c)** (H , T) MPD determined by neutron diffraction experiment for a magnetic field applied along the [001] direction. The incommensurate phase of PuSb has the stacking of the (001) planes, with a quasi-wave modulation of the moment value from plane to plane. PuSb is the only one among pure actinide monocompounds to show the IC-phase. In this sense, PuSb is different from cerium and actinide mononictides, which always exhibit commensurate magnetic structures [85RBQV], [88BFPQ].

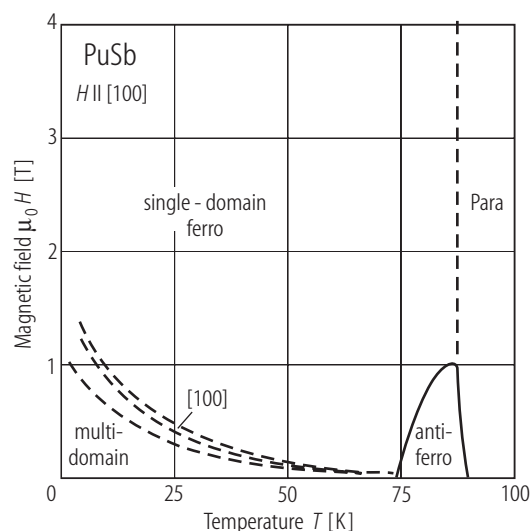


Fig. V.129. PuSb s.c. (H , T) MPD for a case $H \parallel [100]$ [86MVSRI]. Note that at low temperatures the magnetic field first transfers the crystal into a single-domain ferromagnet. The magnetic field strength of an order of maximum 1 T changes the antiferromagnetic structure into induced ferromagnetism at temperature close to T_N ($= 85$ K).

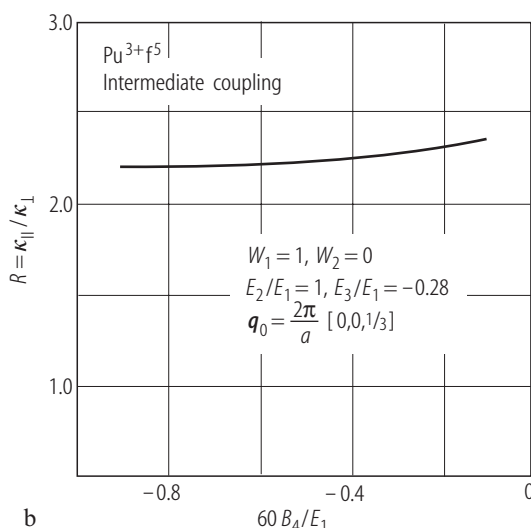
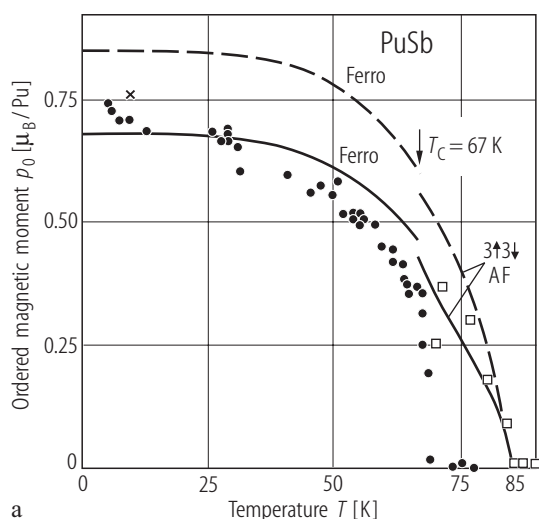


Fig. V.130. PuSb s.c. **(a)** Experimental and theoretical variation of the ordered moment, p_0 , vs. temperature, T , [88HKBC]. The experimental magnetization values are from [84BQRS] (closed points and open squares) and from [84LDBS] (the cross). The dashed and solid curves are the predicted temperature variation of magnetization for i) the IC case with $E_2 = E_1$, $E_3 = -0.279 E_1$ and $60 B_4 = -0.31 E_1$. $E_1 = 149.1$ K-to match the experimental value of $T_N = 85$ K and for ii) the L - S coupling case with $E_2 = E_1$, $E_3 = 0.306 E_1$, $60 B_4 = -0.38 E_1$ and $E_1 = 121.4$ K. The calculations were made by including the next-to-dominant single-site scattering processes involving f -electrons in $m_l = \pm 1$ and

$m_s = \pm 1/2$ states. **(b)** Theoretical ratio of inverse correlation lengths, R ($= \kappa_{||}/\kappa_{\perp}$) calculated for parameters characteristic for PuSb (indicated) as a function of the ratio of the crystal field parameter $60 B_4$ to the nn anisotropic exchange parameter E_1 . W_1 and W_2 are the phenomenological weighting factors, which provide the ratio of contributions to the strength of two-ion interaction (for explanation see [87CHKW]). This is for the case of a longitudinally polarized AF structure in the IC scheme. All these provide *equilibrium* behaviour of PuSb approximating the experimental behaviour rather to parameters almost independent of CEF parameters [88HKBC].

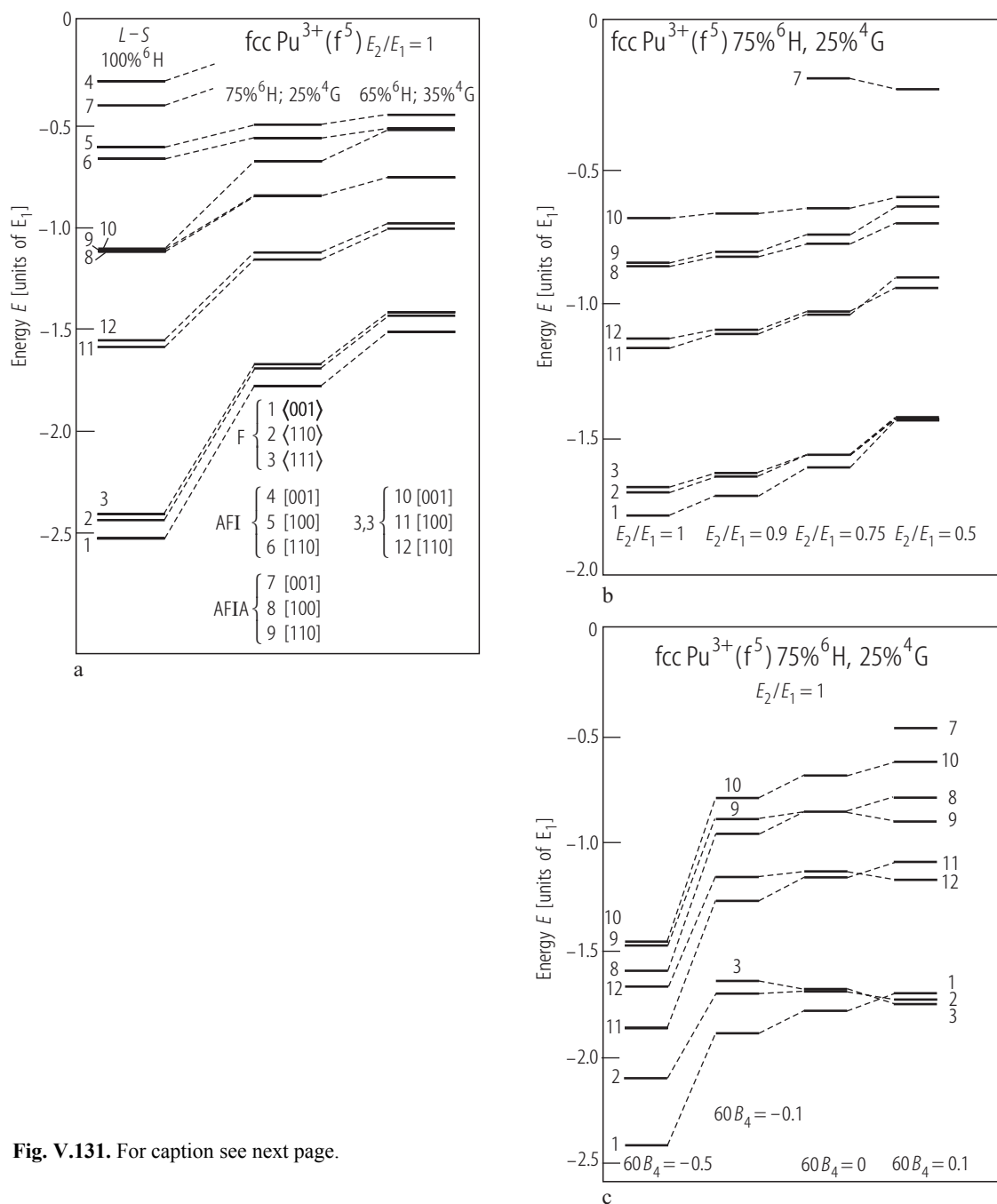


Fig. V.131. For caption see next page.

Fig. V.131. PuSb. Free energies at $T = 0$ K of different magnetic structures, calculated on the basis of an anisotropic hybridization-mediated two-ion interaction model using the phenomenological parameters E_n (see the Introduction) [84BCT]. The calculations were made for the cases of L - S coupling and intermediate coupling (IC) for two ground terms suitable for the Pu^{3+} ion ($5f^6$) in PuSb. They are: i) 75% ^6H and 25% ^4G and ii) 65% ^6H and 35% ^4G (see figure a). The structure AF ($3+, 3-$) is here included, which should be more closer to the ferromagnetic state, due to the increase of the number of ferromagnetic planes with the equally directed up or down. For each magnetic structure type three different configurations are considered. As seen, there is not a drastical difference in the behaviour of the IC system from that of the L - S system. Nevertheless, the difference exists in respect to some experimental findings. It occurs that the long period (LP) AF structure to which the ferromagnetic arrangement undergoes (e.g. $(3+, 3-)$), instead of a longitudinal polarization indicated by experiment [84BQRS], has the transverse ($\mathbf{q} \perp \mathbf{p}_0$) one. The effect of changing the ratio E_2/E_1 on the composition of the ground-term is shown in figure (b). Figure (c) shows for the case $E_2/E_1 = 1$ the different types of magnetic structures depending on varying values of the crystal field parameter B_4 [84BCT], defined in [62LLW]. ($B_4 = -(1.3/60)E_1$, $E_1 = 129.8$ K).

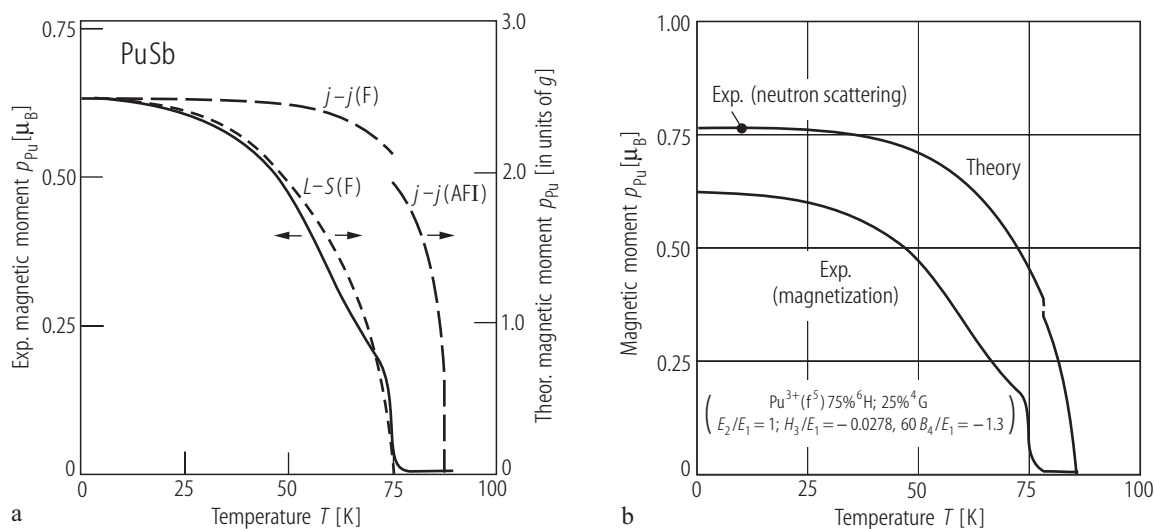
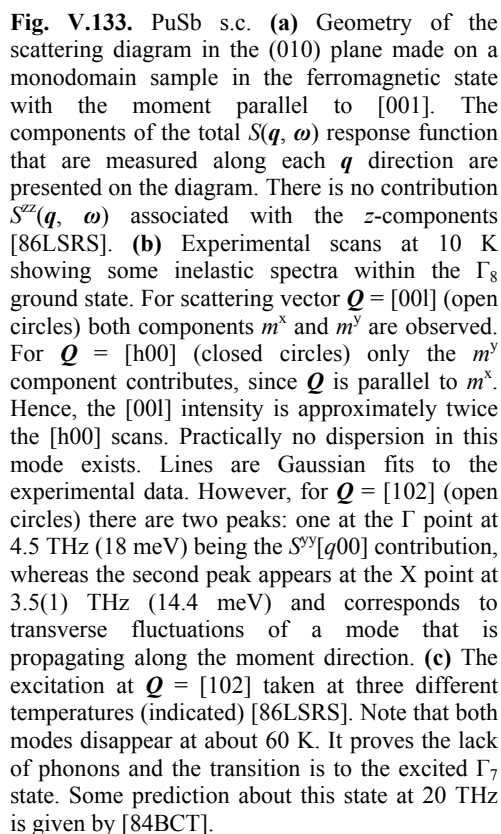
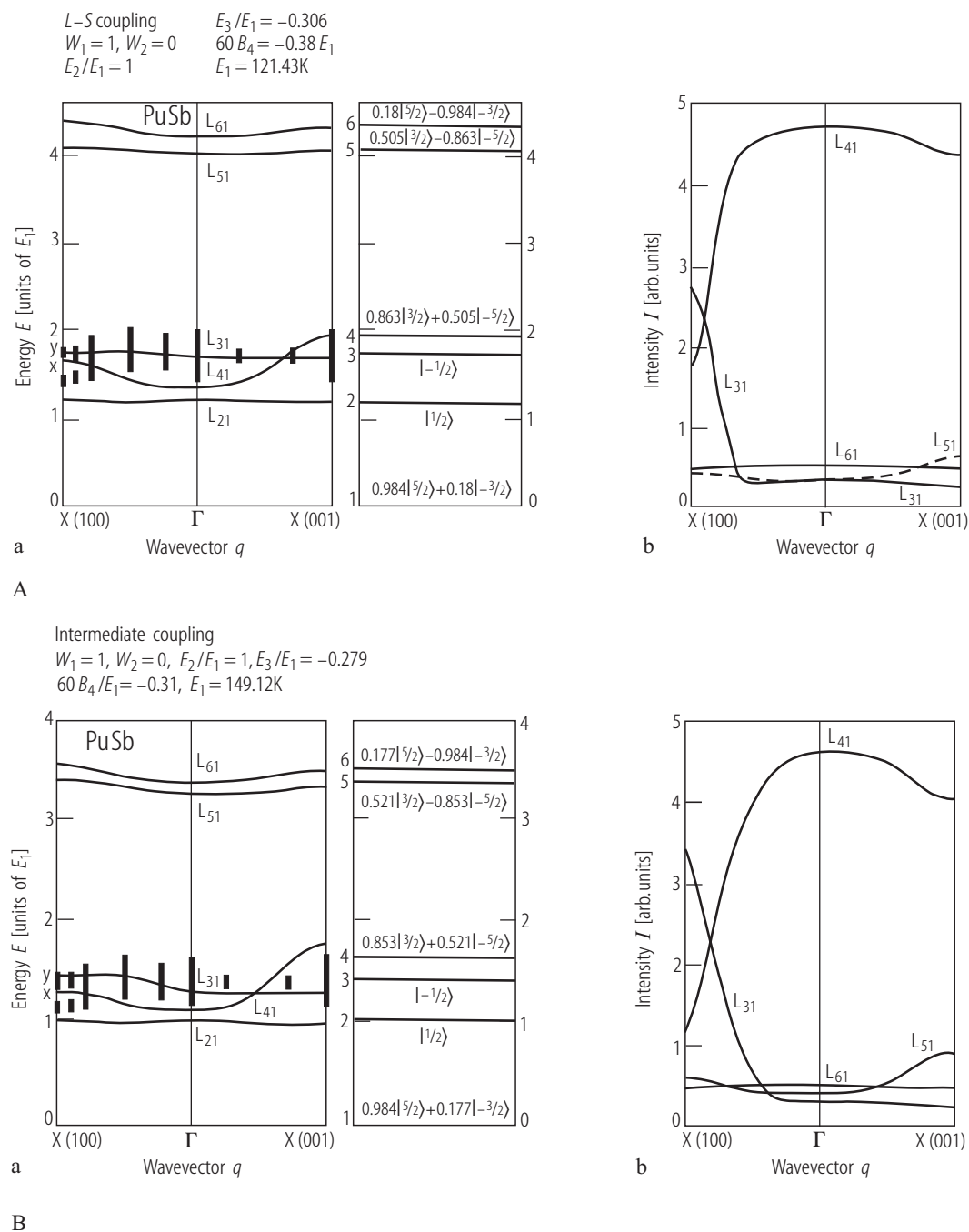


Fig. V.132. PuSb. (a) A comparison of the experimental magnetic moment, p_{Pu} , vs. temperature, T , (solid curve) with theoretical curves of Pu^{3+} in PuSb for two CF approaches 1) L - S (short-dashed line) and 2) IC (j - j) (long-dashed line) [83CTSM]. The g values for L - S and j - j coupling are $2/7$ and $6/7$, respectively, [84TC1]. As seen, the L - S model gives better agreement with experiment, while the j - j model reproduces the first order F-AF I transition. However the

value of an ordered moment is just like that for Ce^{3+} ($g = 6/7$). (b) The comparison of theoretical with experimental results is shown, where the fitting of the moment size to that found by neutron scattering (closed point) [84LDBS] has been made. This requires to include a large crystal field with the Γ_8 level pushed to the energy lower than the Γ_7 level by applying the hybridization dressing [84BCT].





B

Fig. V.134. PuSb. Dispersion curves calculated for two cases: **(A)** *L-S* and **(B)** *IC* schemes compared with experiment [88HKBC]. **(a)** On the left hand panels A and B: an excitation magnetic behaviour in the ferromagnetic phase at $T = 0$ for q along the [100] and [001] directions, i.e. perpendicular and parallel to the moment direction, respectively, developed on the basis of the theory presented in Refs. [84BCT], [86CBKW], [87CHKW], [95LSC]. L_{31} , L_{41} and L_{51} label transverse modes, while L_{61} and L_{21} are longitudinal and quadrupolar modes, respectively. Heavy vertical bars are experimental results of

[86LSRS], found at 10 K, and using 0.5 cm^3 single crystal, see Fig. V.135b. Note, that almost dispersionless magnetic transitions with an energy of 4.3 MHz are apparent. On the right hand panels A and B: the energy levels of the molecular-field states and their compositions. **(b)** Relative intensity of the modes presented in figures **(a)**. The intensity of quadrupole mode L_{21} is zero [88HKBC]. Note that the strong mixing of the transverse modes L_{31} and L_{41} leads at the zone boundary to two experimentally found modes presented in Fig. V.135b (see there two peaks). For E_i, W_i see Fig. V.130

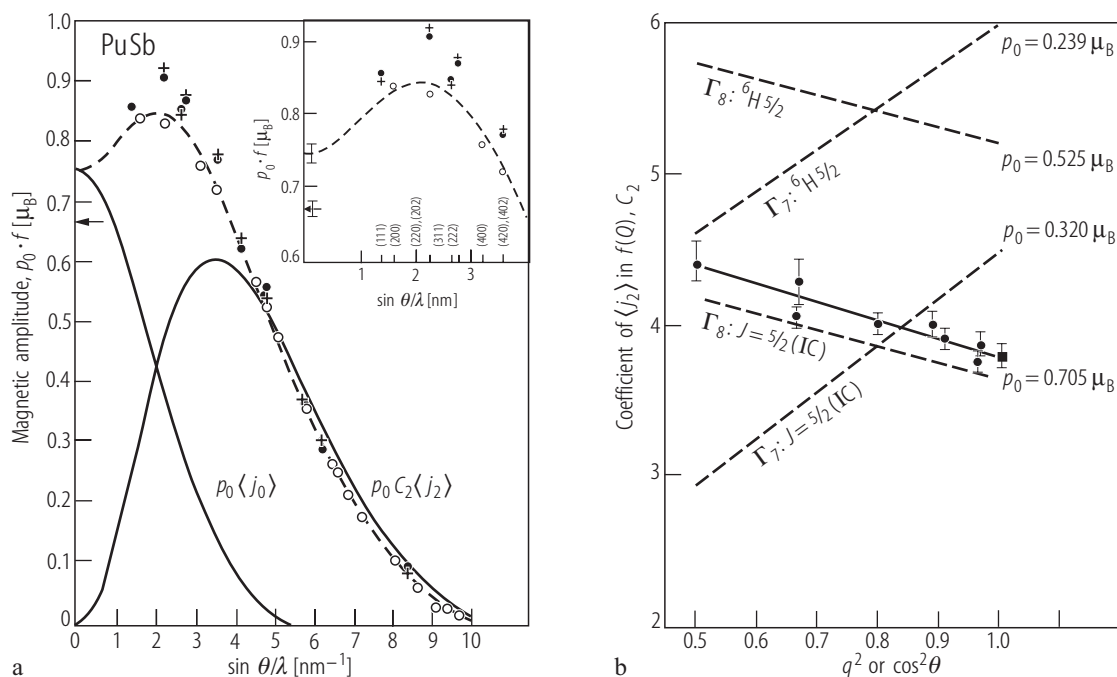


Fig. V.135. PuSb s.c. Polarized neutron experiment at 10 K: **(a)** Experimental form factor $f(\mathbf{Q})$ multiplied by p_0 (\equiv magnetic amplitude) measured in the plane perpendicular to the moment (open circles) and out of this plane (closed circles) as a function of the scattering vector $\mathbf{Q}/4\pi$ ($= \sin \theta / \lambda$) [84LDBS, 85LDBS, 87L2, 88LWRS]. Inset: the low-angle part giving more details [87L1]. The dashed line is the calculated $f(\mathbf{Q})$ for the points in the scattering plane, while crosses are calculated points for the out of the scattering plane case. The anisotropy, for example between (202) and (220) points defines the *oblate* nature of the magnetization density and suggests a Γ_8 ground-state wave function (see figure b) of Pu^{3+} . The smooth curve $p_0 \langle j_0 \rangle$ is the spin-only contribution, whereas $p_0 C_2 \langle j_2 \rangle$ describes a large orbital moment contribution (see the Introduction). The fact that the maximum in $p_0 f(\mathbf{Q})$ is reached not at $Q = 0$ but at $Q \approx 0.2 \text{ \AA}^{-1}$ is a strong signature for a trivalent plutonium ground state. This arises because of almost cancellation of the orbital and spin moments being both large and oppositely directed ($\mathbf{J} = \mathbf{L} - \mathbf{S}$). The arrow gives the moment

derived from bulk magnetization [83CTSM]. **(b)** The coefficient values C_2 and ΔC_2 , which describe the magnetic amplitude (see the Introduction) in the relation: $p_0 f(\mathbf{Q}) = p_0 [\langle j_0 \rangle + (C_2 + \Delta C_2 \sin^2 \theta) \langle j_2 \rangle + C_4 \langle j_4 \rangle]$, calculated for different CEF ground states are plotted against θ . The term $\Delta C_2 \sin^2 \theta$ takes into account the fact of existence of a quadrupole moment in the magnetization density (θ is the azimuthal angle between the direction $\mathbf{p}_0 \parallel [001]$ and other directions of interest). As seen, the $\Gamma_8(\text{IC})$ wave-function of the ground term ${}^6H_{5/2}$ with $p_0 = 0.705 \mu_B$, $C_2 = 3.62$ and positive ΔC_2 becomes a good representation of the experimental data (closed circles). This is a quite opposite result to that in the lanthanide NaCl compounds, which have the Γ_7 level (negative ΔC_2) as a ground state. The observed difference arises from much stronger mixing of the 5f electrons, with the valence p-bands compared to the 4f electrons [82TTYK]. Also the hybridization effects [83CTSM], [88HKBC] drive the Γ_8 state lower in energy compared to the Γ_7 state. $p_0 = 0.745(20) \mu_B$, $C_2 = 3.80(7)$, $\Delta C_2 = 1.30(15)$ and $C_4 = -0.21(7)$ [84LDBS].

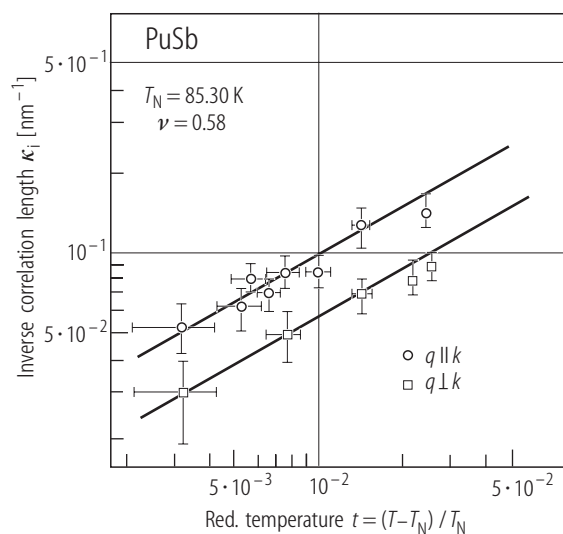
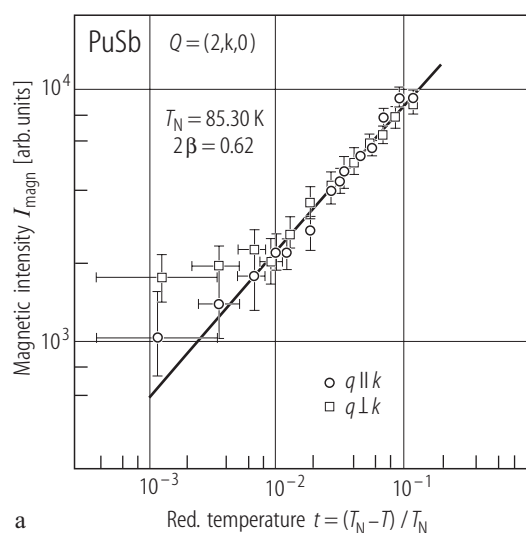
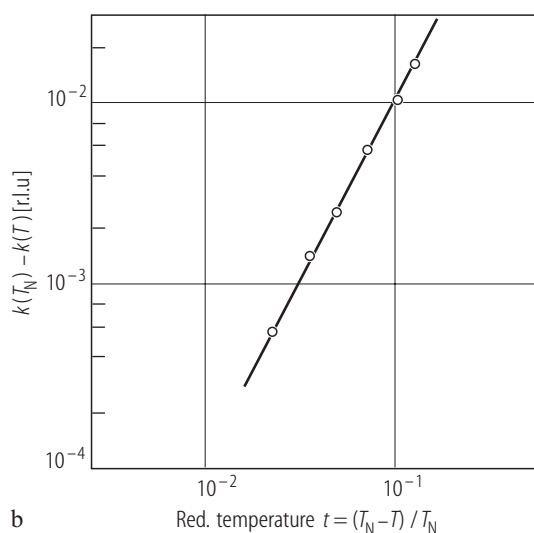


Fig. V.136. PuSb s.c. The inverse correlation length, κ_i , vs. reduced temperature, t , measured above T_N [89BQRS]. Values for κ_{\perp} and κ_{\parallel} correspond to scans q made parallel and perpendicular to the wave vector k . $R = 1.8(2)$. $\nu = 0.58(5)$ where $\kappa_i \sim t^{\nu}$, (see Figs. IV.105 and 106).



a



b

Fig. V.137. PuSb s.c. DCNS: **(a)** Magnetic intensity, I_{magn} , vs. reduced temperature, t , ($= (T_N - T)/T_N$) below T_N ($= 85.3(1)$ K) on a double logarithmic plot [87BRLS]. $\beta = 0.31(2)$. This value is almost like that in USb ($0.32(2)$) and in good agreement with 3D Ising solution of $5/16 = 0.3125$. **(b)** The wavevector function, $k(T_N) - k(T)$, vs. reduced

temperature, t , measured below T_N within the incommensurate (IC) antiferromagnetic phase [87BRLS], $k(T_N) - k(T) = a (T_N - T)^n$. $k(T_N) = 0.131(1)$ r.l.u., but the exponent $n = 2.0(2)$ rather than ~ 3 presented in Fig. V.130a. No signaling about some squaring of the sine wave modulation has been found.

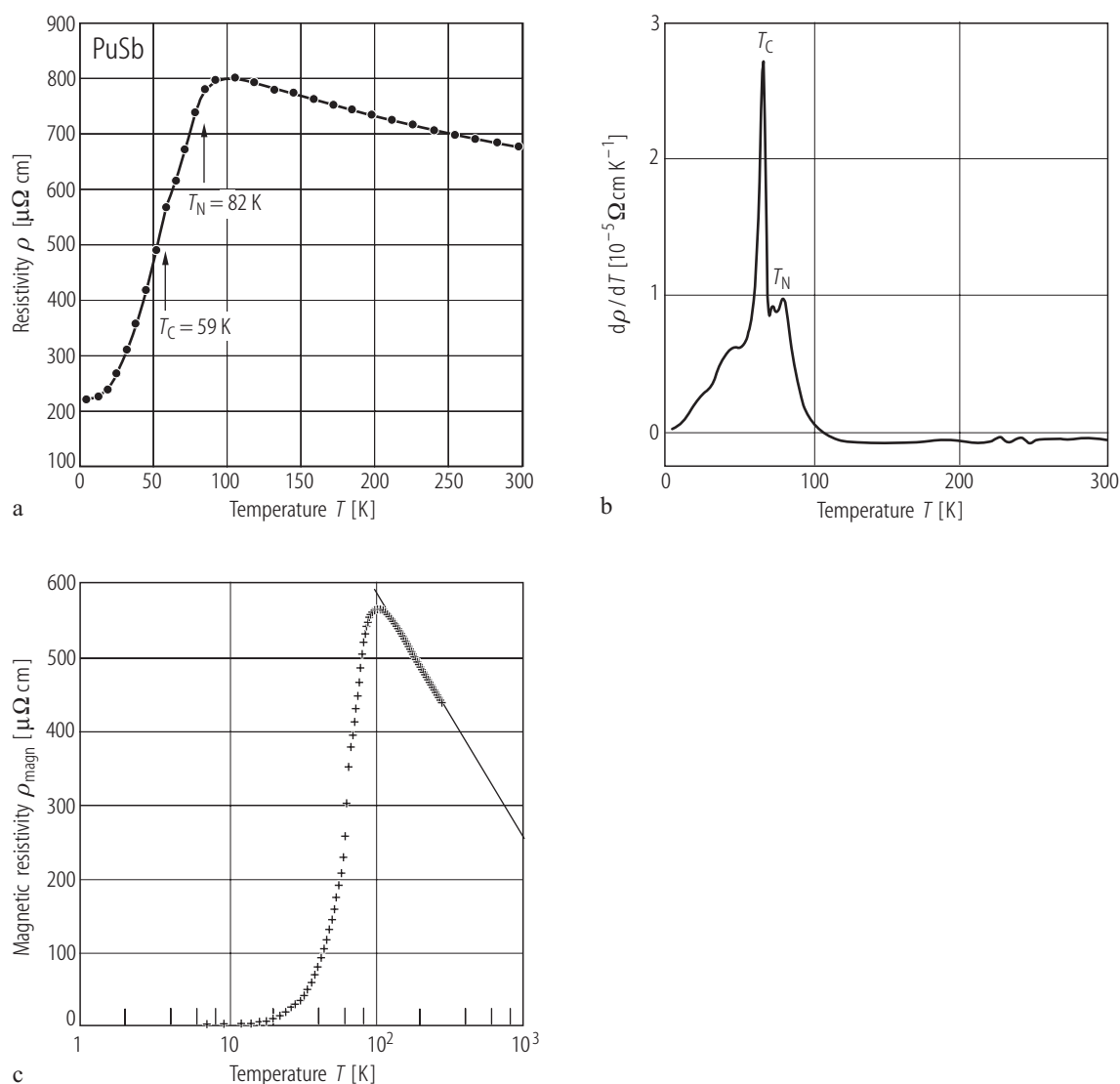


Fig. V.138. PuSb s.c. **(a)** Electrical resistivity, ρ , vs. temperature, T , between 4.2...300 K measured along two directions [100] and [111] on two samples, respectively. No anisotropy was detected [85BCFR]. The onset of magnetic ordering is only reflected by a rapid increase of $\rho(T)$ in the vicinity of 79 K (or 82 K [93FG]). $\rho(T)$ is then passing through a broad maximum centered at 106 K. The temperature of the maximum is an indication of the overall

crystal field splitting, Δ_{CF}/k_B 100 K. **(b)** $d\rho(T)/dT$ vs. T . In contrast to $\rho(T)$, the anomaly at 64 K in $d\rho(T)/dT$ is here well seen as a sharp maximum [85BCFR]. **(c)** ρ_{magn} vs. $\log T$. The magnetic contribution to the resistivity was derived by taking $\rho_{\text{ph}} = aT$, $a = 0.085\text{ }\mu\Omega\text{ cm/K}$, from $\rho(T)$ of ThSb [82FSVA]. Below T_N : $\rho_{\text{magn}} = bT^2$ at least between 15...51 K, $b = 0.027\text{ }\mu\Omega\text{ cm/K}^2$, while above T_N : $\rho_{\text{magn}} = \rho_M(1 - c\log T)$, $\rho_M = 1266\text{ }\mu\Omega\text{ cm}$ and $c = 0.11$ [85BCFR].

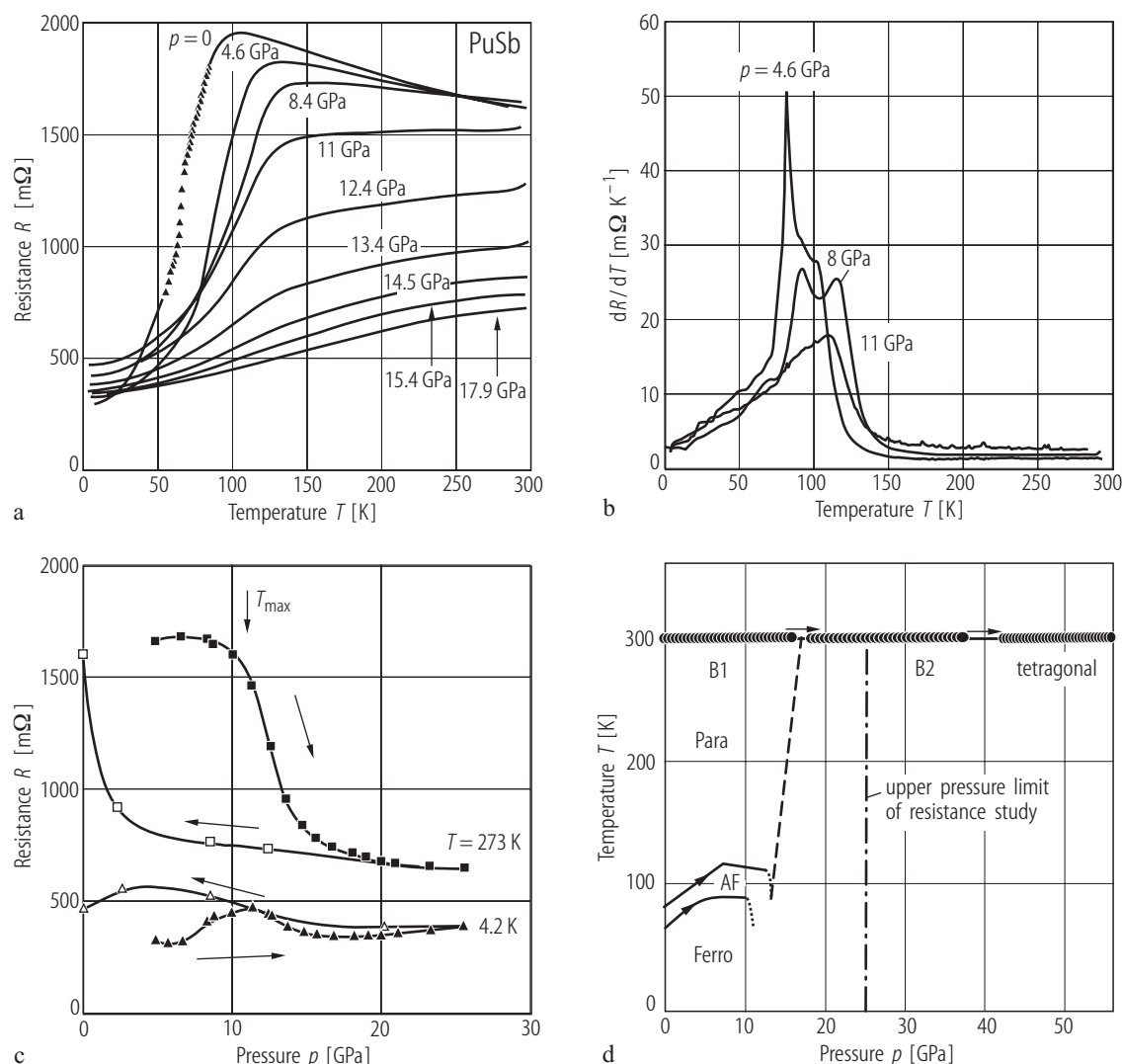


Fig. V.139. PuSb s.c. **(a)** Electrical resistance, R , vs. temperature, T , measured at several values of pressure, p , from 0 to 17.9 GPa [94LBWW]. The curve taken at ambient pressure is from [85BCFR]. Note that the maximum (or shoulder) in $R(T)$ indicates the Néel temperature T_N which increases from 82 to 112 K with increasing pressure. Note also that in the pressure range 10...15 GPa, the electrical resistance, R , decreases rapidly at higher temperatures, while at lower temperatures R reaches a maximum value at ~ 12 GPa. The most important change at higher temperatures is a slow-down disappearance of a Kondo-like behaviour with pressure with simultaneous increase of transition temperature ($R(T)$ -maximum). **(b)** The low-temperature derivative of the resistivity, dR/dT , taken at three pressure

values (indicated) [85BCFR]. The low-temperature peak is associated with the temperature of transition from IC-AF to ferromagnetic phases, which increases from 65 to 80 K with increasing pressure. Note that above 8 GPa this transition disappears [94LBWW]. **(c)** R vs. p at 273 K (upper curve) and 4.2 K (lower curve) for increasing (closed symbols) and decreasing (open symbols) pressures [94LBWW]. Note a maximum in $R(p)$ at 12.5 GPa in the 4.2 K-curve and hysteretic behaviour for both dependences. All those profound changes are caused by the crystallographic phase transitions (see figure d). **(d)** Structural and magnetic phase diagram [94B]. Arrows indicate the direction of pressure change (for understanding see figure a).

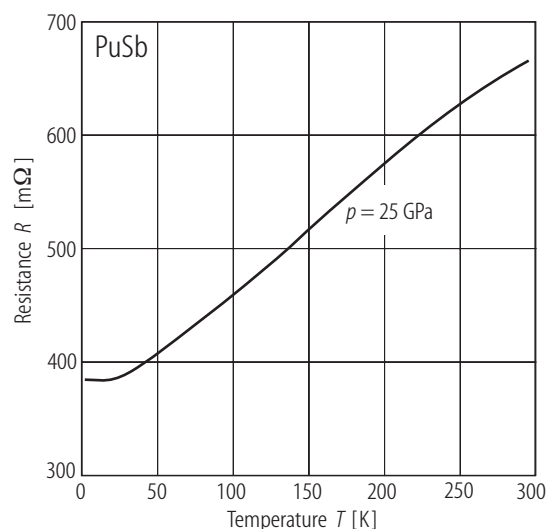


Fig. V.140. PuSb s.c. Electrical resistance, R , vs. temperature, T , measured under the highest available pressure of 25 GPa [94LBWW]. Note an exponential change of $R(T)$ below 20 K and an almost linear dependence above this temperature. No indication of any magnetic order is apparent. An explanation of this fact is possible if one takes into consideration that the 5f-electron delocalization occurs under pressure, in contrast to the X-ray high-pressure conclusions (see Fig. V.125).

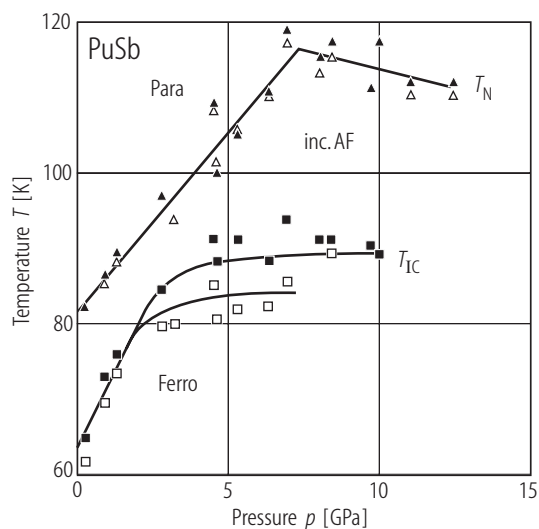


Fig. V.141. PuSb s.c. (T, p) MPD, derived on the basis of electrical resistance R vs. p measurements [94LBWW]. Closed and open symbols are for increasing and decreasing pressure values.

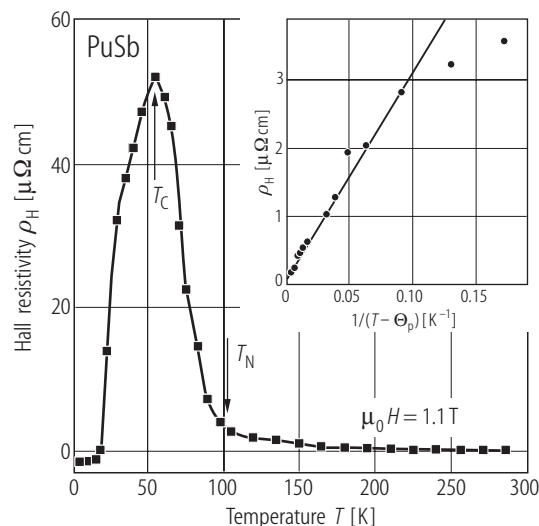


Fig. V.142. PuSb s.c. Hall resistivity, ρ_H , vs. temperature, T , [87TBFR]. Note that the drop of ρ_H to a negative value takes place at low temperatures. This corresponds to a coercive field becoming larger than the applied field when cooling down the sample, first below T_N (≈ 85 K) and then below T_{IC} (≈ 63 K) where an IC structure locks in a ferromagnetic phase. Inset: ρ_H vs. $(T - \Theta_p)^{-1}$, where Θ_p is the paramagnetic Curie temperature. The ρ_H vs. B dependence at 4.2 K (not shown) is a straight line yielding R_0 (the normal Hall effect) of $-0.6 \mu\Omega\text{cm/T}$, i.e. the conduction mainly originates from electrons.

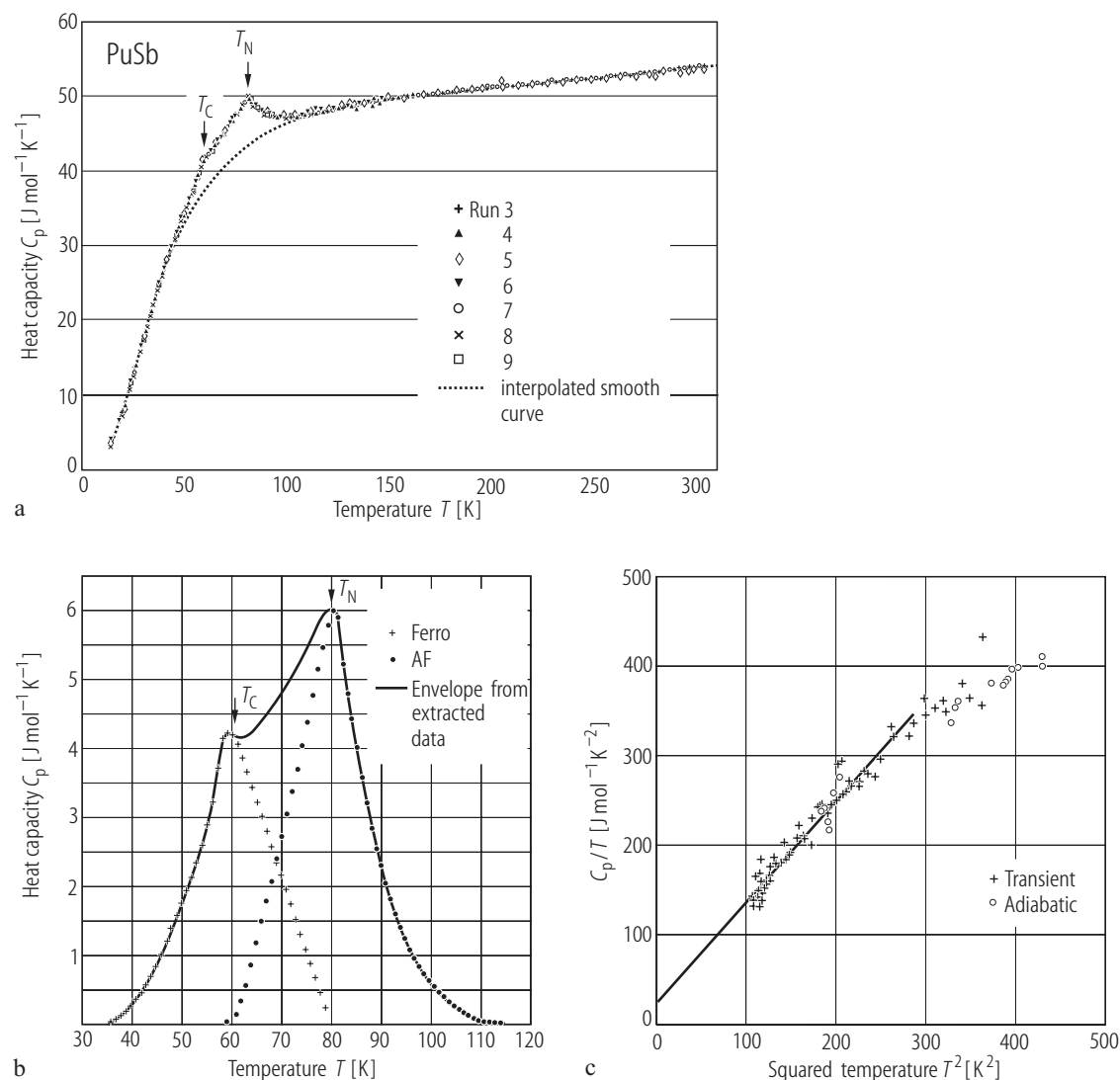


Fig. V.143. PuSb s.c. **(a)** Heat capacity, C_p , vs. temperature, T , measured between 13...300 K [86HJMS]. As many as 9 adiabatic runs were performed. No divergence between various runs for a wide range of heating rates was observed. Note a small C_p excess at about 60 K due to a transition to ferromagnetic state and a C_p peak at 80 K due to a second-order transition to antiferromagnetic state. **(b)** A separation of the C_p anomaly into two peaks at 58 K and 79 K. The transition temperatures are lower than those derived from

magnetic and neutron diffraction experiments namely 67(75 K) and 85 K [83CTSM] and [84BQRS], respectively. The associated minimum values of entropies $S_M = 1.30$ and 1.40 J/mol K, respectively [86HJMS]. **(c)** The C_p/T vs. T^2 plot. The C_p data below 20 K were obtained by two methods, adiabatic and transient, estimated with absolute errors of 0.5 and 1.5%, respectively. Extrapolation of C_p/T from the lowest temperature of 10 K to zero K yields $\gamma(0) = 20(10)$ mJ/mol K², $\Theta_D = 151(10)$ K [86HJMS].

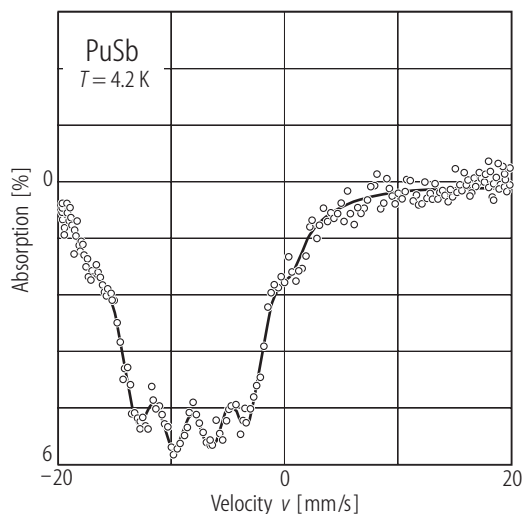


Fig. V.144. PuSb. ^{121}Sb Mössbauer spectra at 4.2 K [87SSRV]. Two mechanisms contribute to the transferred hyperfine field of ^{121}Sb : 1) the conduction electron polarization (RKKY-interaction), and 2) the mixing 5f with 5sp-electrons of the Sb atoms. The ^{121}Sb hyperfine fields at 4.2 K and other parameters required to calculate transferred Mössbauer spectra in the Sb-containing actinide monocompounds are given in the Table below:

	USb $\text{U}^{3+}(5f^3)$	NpSb $\text{Np}^{3+}(5f^4)$	PuSb $\text{Pu}^{3+}(5f^5)$
Ordering type (4.2 K)	AF-I	AF-I	F
$\Sigma p_0/p_0$ *)	2	2	6
p_0 [μ_B]	2.82(5)	2.5(1)	0.75(10)
$p_{\text{An}^{3+}}$ [μ_B]	3.27	2.46	0.86
$(g-1)J$	-1.23	-1.54	-1.64
$\mu_0 H_{\text{hf}}$ [T]	17.1(4)	16.4(4)	21.5(4)
$\mu_0 H_s$ [T]	4.0	2.7	1.25

*) This represents the weighed vector sum of the magnetic moments in the immediate vicinity of the Sb atoms

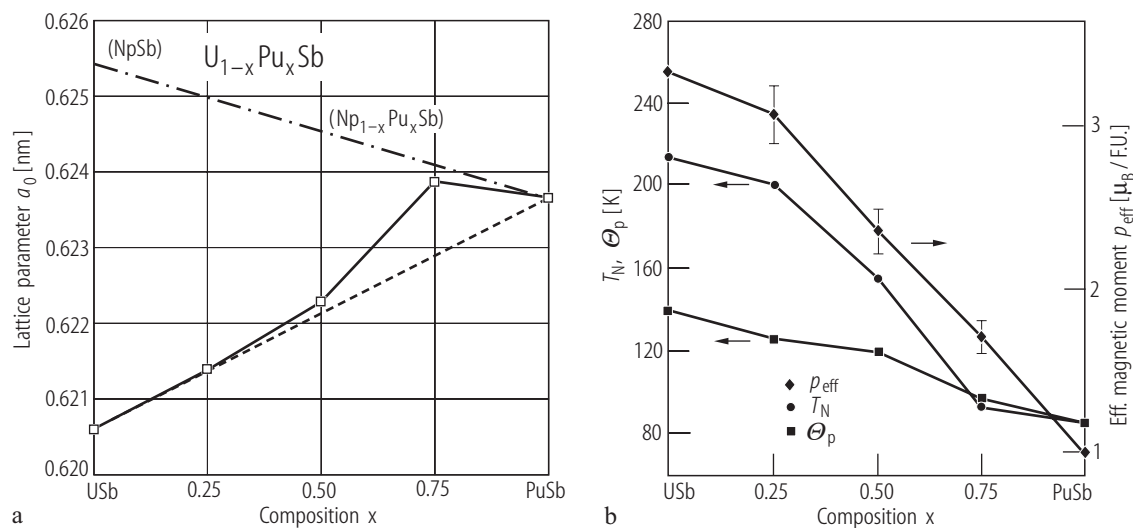


Fig. V.145. (U, Pu)Sb s.c. (a) Lattice parameters, a_0 , vs. composition, x , for the solid solutions $\text{U}_{1-x}\text{Pu}_x\text{Sb}$ [98RWRB]. (b) The magnetic parameters, T_N , Θ_p (lhs), and p_{eff} (rhs), as a function of Pu concentration, x , [02KWRL].

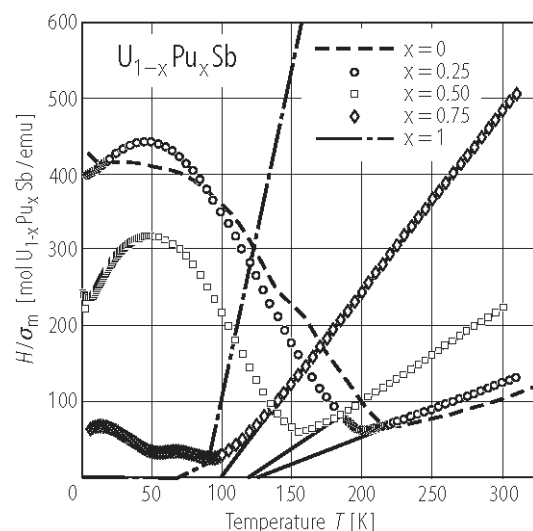


Fig. V.146. (U,Pu)Sb s.c. The ratio H/σ_m vs. temperature, T , measured for the solid solutions $U_{1-x}Pu_xSb$, with $x = 0.25$, 0.50 and 0.75 in an applied field of 1 T [02KWRL]. For comparison the data for USb and PuSb, taken from [98VMLR], are included as dashed and dot-dashed lines, respectively. At temperatures higher than T_N the data follow a CW law, represented by solid lines. For magnetic characterization of the solid solution see also the Table below.

x	T_N [K]	Θ_p [K]	p_{eff} [μ_B/FU]
0.25	200	126	3.35
0.50	155	120	2.54
0.75	93	97	1.82

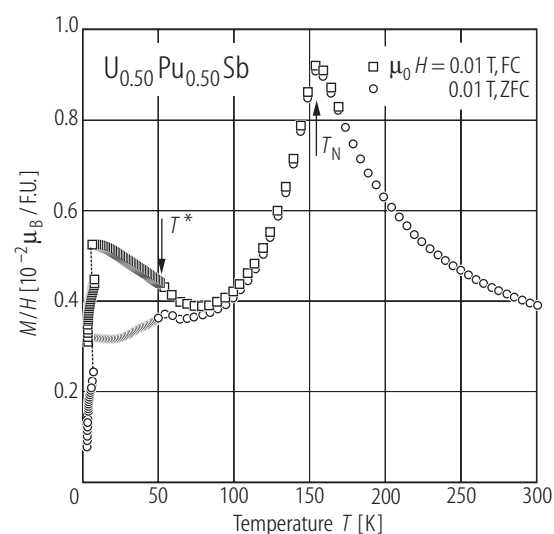


Fig. V.147. (U, Pu)Sb. s.c. The M/H ratio (in μ_B/FU) vs. temperature, T , for the solid solution $U_{0.5}Pu_{0.5}Sb$ [02KWRL]. $T_N = 155\text{ K}$. The triple- k ($k = 1$) magnetic structure, characteristic for USb and NpSb, is stable in the concentration range of $x \approx 0.50$ (see also [02NSML1]). Note the difference in ZFC magnetization data compared to the FC curves below $T^* = 55\text{ K}$.

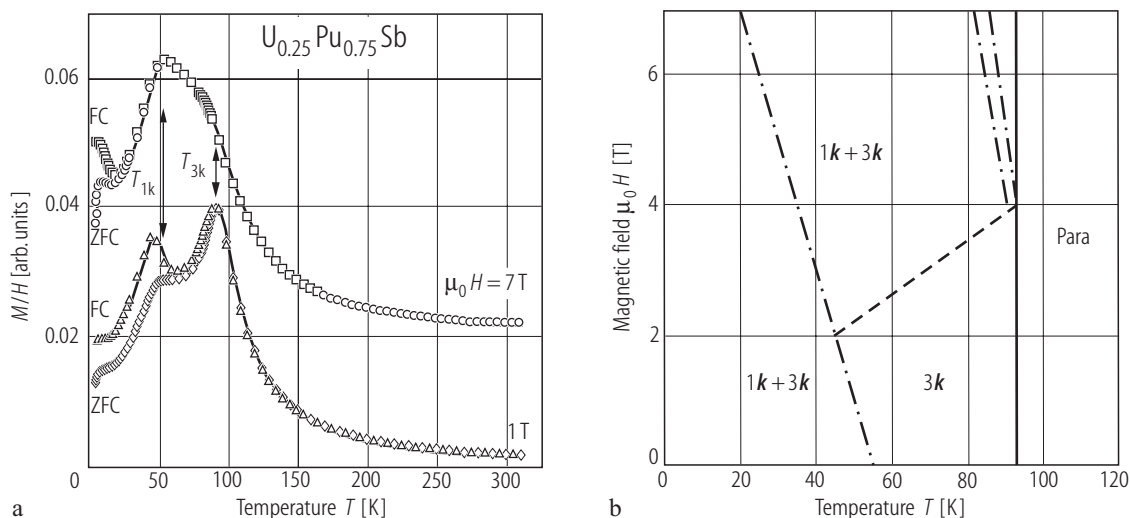


Fig. V.148. (U, Pu)Sb s.c. **(a)** The ratio M/H vs. temperature, T , for the solid solution $U_{0.25}Pu_{0.75}Sb$ taken at 1 and 7 T [02KWRL]. There are two transitions in the ordered state, one at 93 K into the AF- $3k$ structure and the second at 55 K into the AF- $1k$ structure. For both structures $k = 0.25$ rlu., i.e. a $(4+4-)$ -type structure. **(b)** (H, T) MPD for $U_{0.25}Pu_{0.75}Sb$ on the basis of magnetization (transition lines) [02KWRL] and neutron (assignment of structures) [02NSML1,2] studies. The three dot-dashed lines are a consequence of the random distribution of the two types of magnetic ions carrying different values of ordered

moments. This leads to the so-called *random-field effects* (RFE), which in consequence cause some variation in the environment of a given magnetic ion and give rise to different exchange interactions in different directions. As seen, in magnetization measurements the strong field dependence of RFE is observed. Moreover, the Pu-Pu exchange favours a $[100]$ moment alignment, while the U-U exchange favours a $[111]$ one. Two chain-lines represent sudden domain wall motion, connected with the $1-k$ -type structure only (see the text).

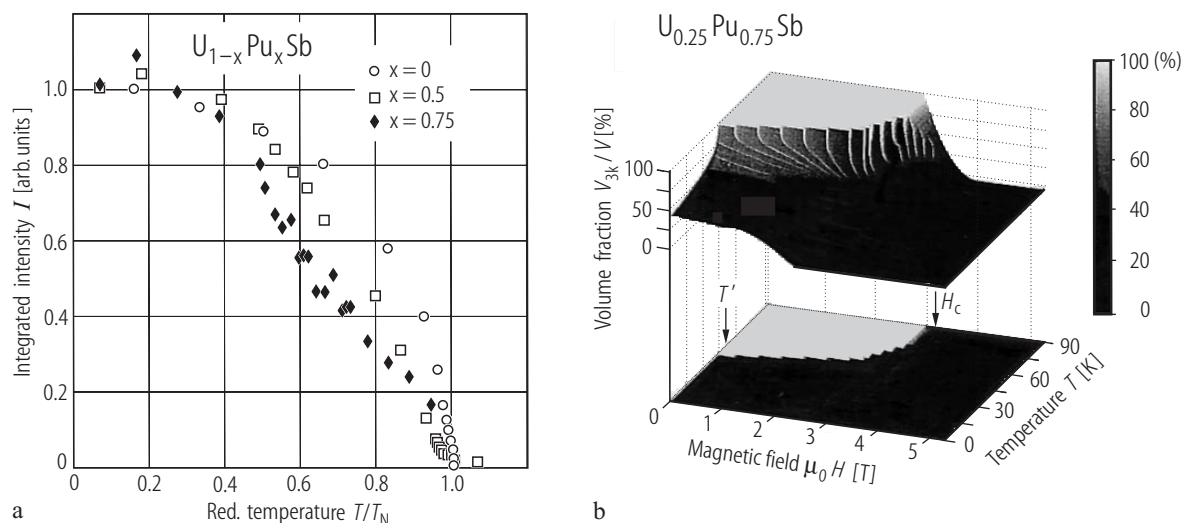


Fig. V.149. (U,Pu)Sb s.c. **(a)** Neutron integrated intensity of the first order harmonics for USb (taken from [76LMSV]) and the solid solutions $U_{1-x}Pu_xSb$ with $x = 0.50$ and 0.75 at $B = 0$ as a function of reduced temperature T/T_N [02NSML1]. For the $x = 0$ and 0.50 samples, the wave vector $k = 1$ and the magnetic structure is AF $1-3k$. For the $x = 0.75$ sample, $k = 0.25$ with partly squaring the modulation. Note a concave dependence of the intensity on temperature in the region $40 < T < 60$ K. **(b)** A schematic (H, T, V)

magnetic “phase diagram” of the solid solution $U_{0.25}Pu_{0.75}Sb$ obtained by integrating the neutron intensities of the three satellites [02NSML1]. This diagram shows the volume percentage of the sample in the $3k$ state. For zero-field the sample transforms from 100% $3k$ at $T_N (= 90$ K) to 30% $3k$ at $T = 0$ K. Note that for high fields the structure is only $1k$, whereas at the lower fields, the sample has the $3k$ -structure down to T' (55 K), and then transforms not-completely

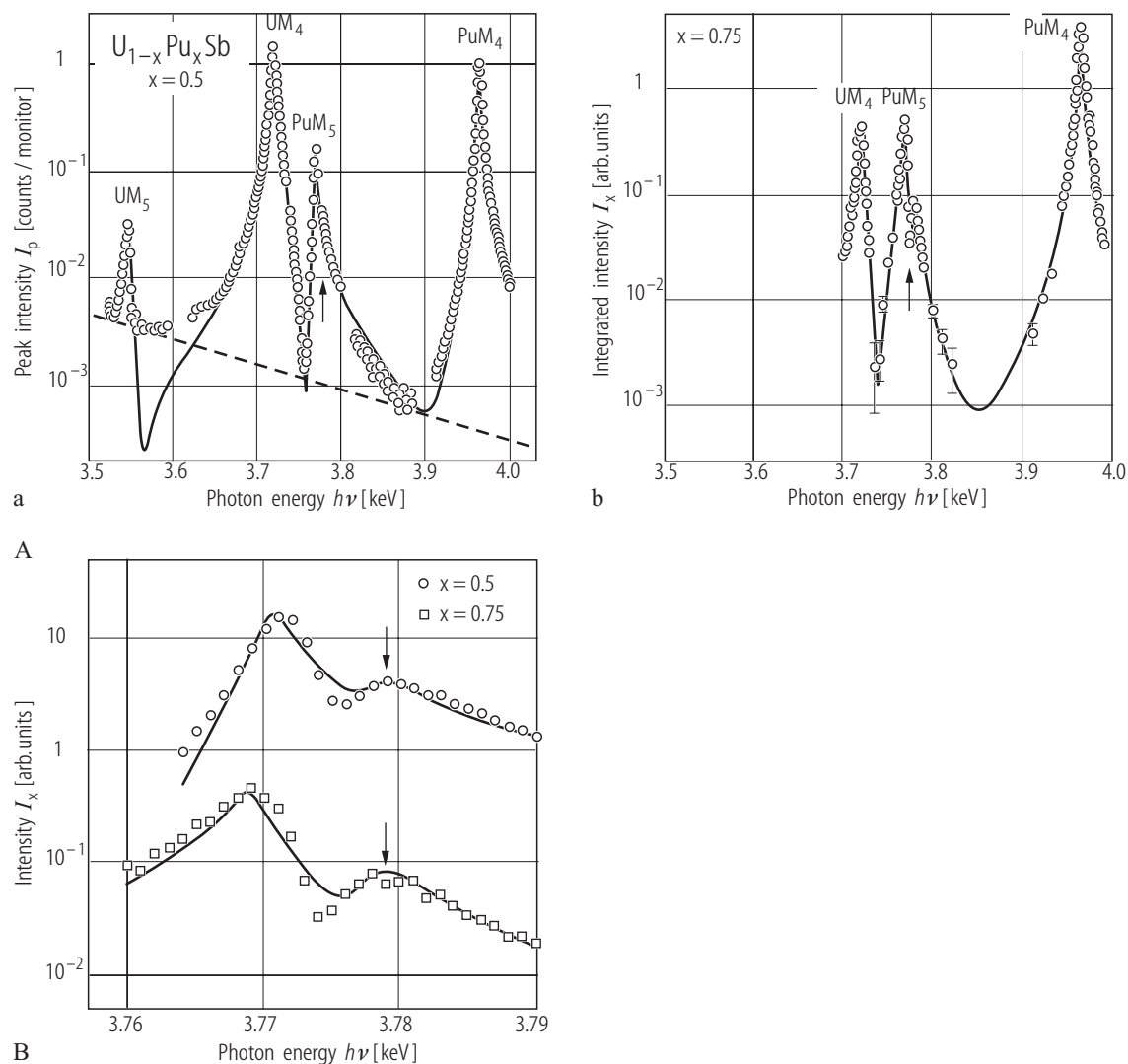


Fig. V.150. $(U,Pu)Sb$ s.c. RXMS: **(A)** Energy spectra. **(a)** The peak intensity of the (003) reflection for the $x = 0.50$ sample (the dashed line represents the background) and **(b)** of the (0, 0.75, 2) reflection for the $x = 0.75$ sample [02NSML2]. Note logarithmic intensity scales and reduced intensity of the U signal for $x = 0.75$ compared to that of the $x = 0.50$ sample. This causes that for $x = 0.75$ the U M_5 energy is not detected. The solid lines are least squares fits of the resonance position, its amplitude and its FWHM. The arrows show an additional resonance (see fig. B). **(B)** Intensity vs. photon energy $h\nu$ for $x = 0.50$ and 0.75. An additional resonance (arrows) which takes

place near the Pu M_5 position (larger peak), is shown on enlarged energy scale [02NSML2]. The solid line is a fit of the Lorentzian functions together with a full correction of self-absorption. The extra resonance is associated with Pu ions, being principally on an electronic state (Pu^{3+} , $5f^6$) in both solid solutions. According to large K-edge enhancements of 4p ions (Ga, As and Se) (see for example Fig. IV.48), there is a similar speculation that the broad p states of Sb, hybridized with the Pu 5f states, together with their partial polarization give rise to splitting of the Pu M_5 edge.

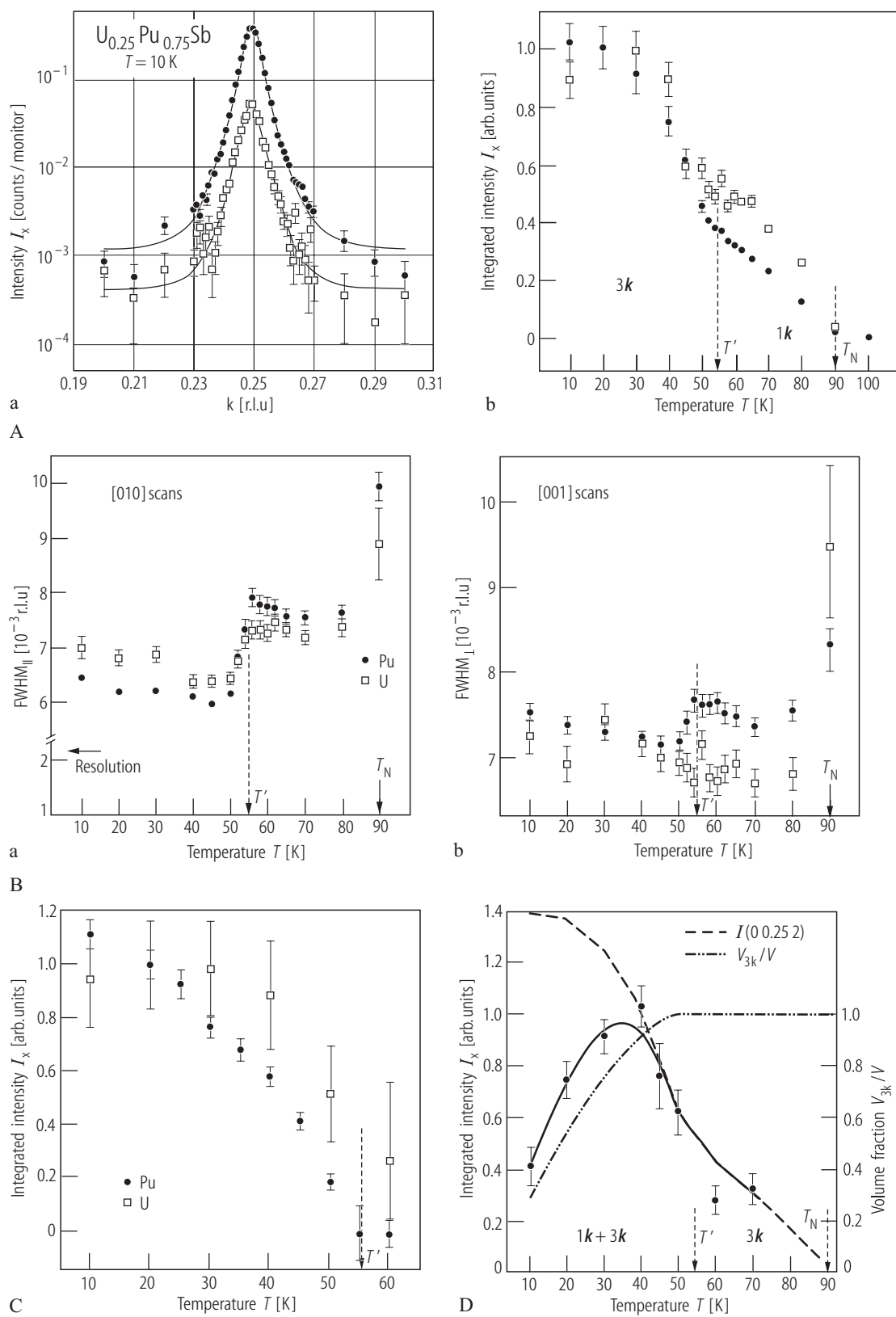


Fig. V.151. For caption see next page

Fig. V.151. (U,Pu)Sb s.c. RXMS: **(A)** (a) Reciprocal lattice scans for $U_{0.25}Pu_{0.75}Sb$ at both the U (open squares) and Pu (closed circles) edges of the $(0, 0.25, 2)$ reflection (1st order harmonic) and **(b)** their temperature dependences of the integrated intensity normalized at 20 K [02NSML1]. The solid lines are fits obtained with Lorentzian squared functions. Note that in **(a)** the intensity is in the log scale and the width of both peaks are similar. The intensity variation with temperature is concave between 40 and 60 K (close to the temperature T^*), which reflects a sluggish transition from a triple- k to a single- k configuration. **(B)** The FWHM of the $(0, 0.25, 2)$ magnetic reflection, being the 1st harmonic one for two directions **(a)** [010] and **(b)** [001] as a function of temperature, T . $T_N = 90$ K. The ordering of both the U and Pu moments is not long range. The correlation length ξ along the longitudinal [010] direction is ~ 400 Å and along the transverse direction is slightly longer (~ 500 Å). This is a highly frustrated system. **(C)** Normalized intensity of the $(0, 0.75, 2)$ magnetic satellite (3rd order harmonic) as a function of temperature, T , [02NSML1]. Open squares – U M_4 edge, closed circles – Pu M_4 edge. Note that the 3rd – order Fourier harmonics disappear at or near T^* , indicating that the squaring exists only within the single- k state. The intensity ratio m_3/m_1 of harmonic satellites is 0.26(5) and 0.28(1) at the U and Pu edges, respectively (the pure square wave has a ratio of 0.41). **(D)** The integrated intensity of the $(0, 0.25, 2)$ reflection at the Pu M_4 edge as a function of temperature for the solid solution $U_{0.25}Pu_{0.75}Sb$ [02NSML1]. The solid fitting line reflects two competing terms shown as the dashed (lhs) and dot-dashed (rhs) curves, which describe the change of magnetic moment with temperature and the fraction of sample volume in the $3k$ phase, respectively. The latter is in accordance with the neutron measurements (compare Fig. V.149a).

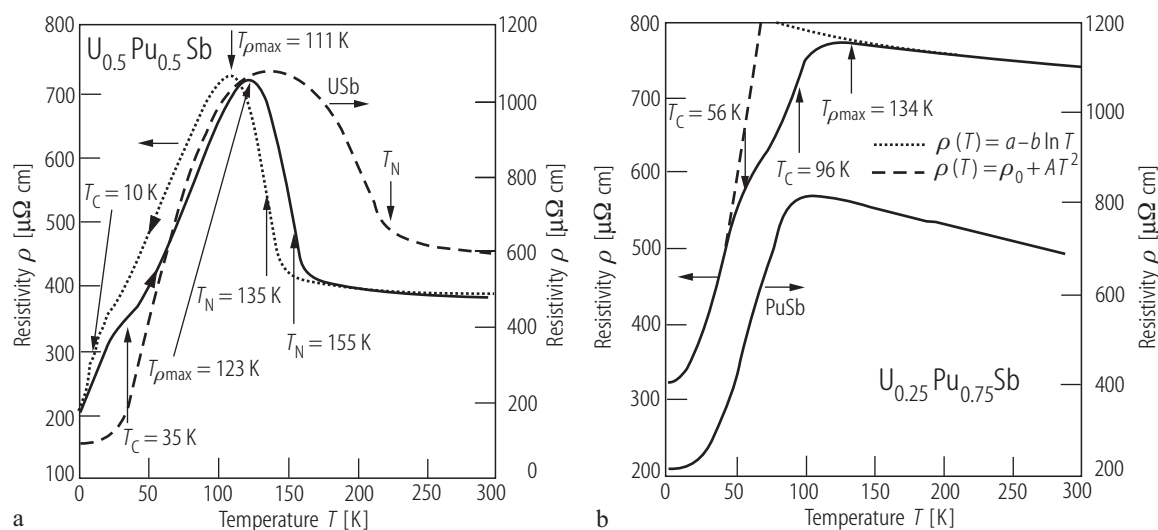


Fig. V.152. (U, Pu)Sb s.c. Electrical resistivity, ρ , vs. temperature, T , for **(a)** $U_{0.5}Pu_{0.5}Sb$ and **(b)** $U_{0.25}Pu_{0.75}Sb$ measured on unoriented single crystals between 1.5...300 K [98RWRB]. In figure **(a)** the ρ vs. T curve for pure USb (taken from [84SFV]) is schematically shown as the dashed line. The solid and dotted curves represent a remarkable hysteresis phenomenon observed in the ordered state. Although the curves present the same features, they are shifted respectively to each other by about 15 K. Note that except for a broad maximum signaling a triple- k magnetic structure and being centered at 123 K for heating and at 111 K for cooling runs, there is also a second anomaly at 35 K and 10 K (see arrows), respectively. This one probably points to a transition into a ferromagnetic state. Instead T^2 or T^4 -type behaviour (as is a case of USb) a rather linear,

non-Fermi liquid behaviour of $\rho(T)$ at low temperatures is observed. In figure **(b)** for comparison the $\rho(T)$ curve for pure PuSb is also shown (right hand scale) [98RWRB]. Note that the resistivity of both curves displays essentially the same features. In $U_{0.25}Pu_{0.75}Sb$ two clear anomalies around 56 and 96 K marked by arrows are seen, which are associated with the ferro- and antiferromagnetic transitions, respectively. Up to 40 K the dependence: $\rho(T) = \rho_0 + AT^2$ ($A = 0.102 \mu\Omega cm/K^2$) is followed (dashed curve). In the paramagnetic state, at first one observes a broad maximum in $\rho(T)$ around 130 K, which is attributed, like for the pure PuSb, to crystal electric field effects, but over 150 K, the dependence: $\rho(T) = a - b \ln T$, where $a = 994 \mu\Omega cm$ and $b = 44.2 \mu\Omega cm/\ln K$, suggests a Kondo-type behaviour.

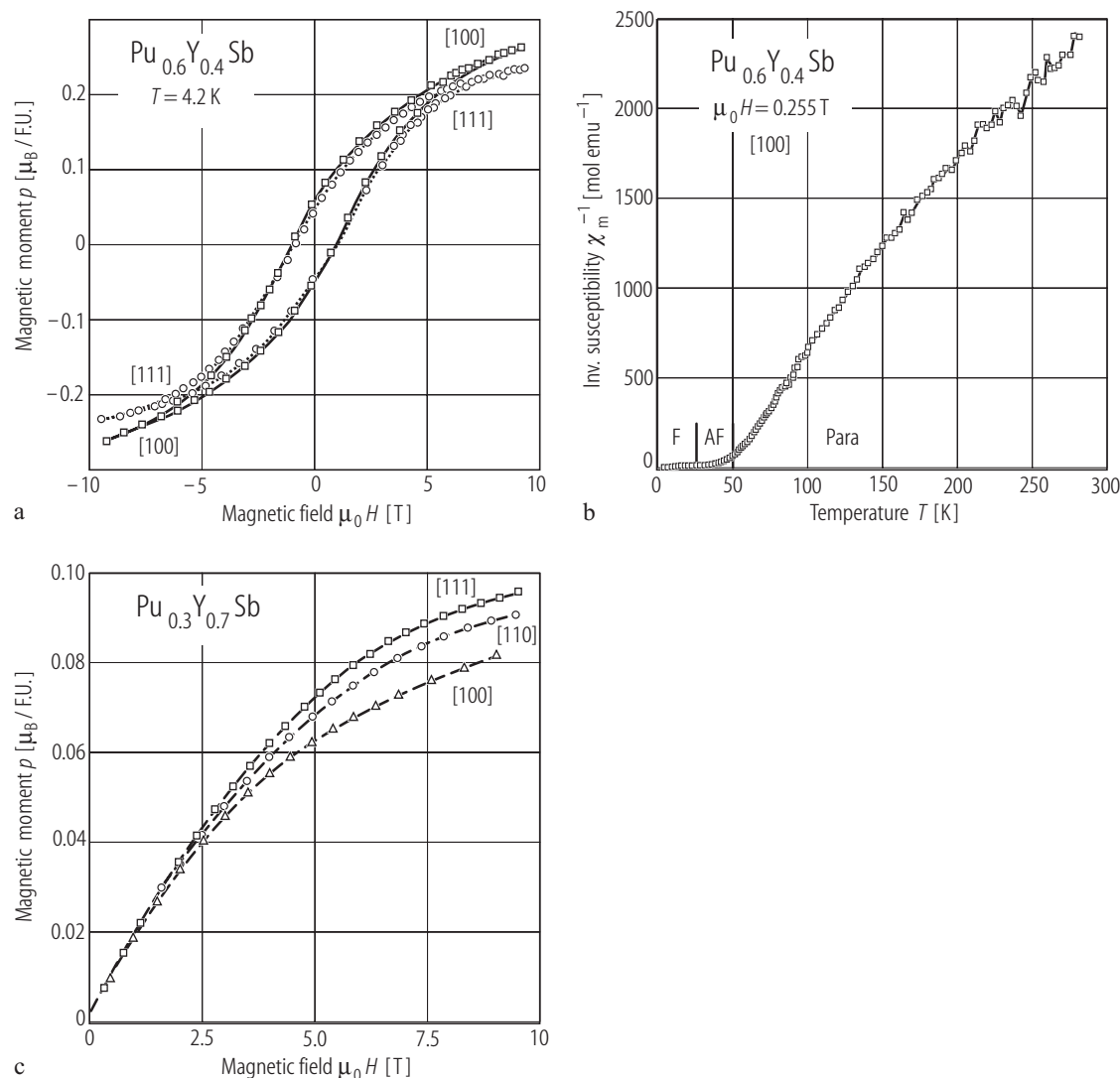


Fig. V.153. (Pu,Y)Sb s.c. (a) Hysteresis loop for the solid solution $\text{Pu}_{0.6}\text{Y}_{0.4}\text{Sb}$ measured along the [100] and [111] directions at 4.2 K [99VLMR]. As seen, the [100] direction is still the magnetization easy axis. The fact, that the coercive field is the smallest along [111] direction favours slowly this axis to be the easy one. (b) Inverse molar magnetic susceptibility, χ_m^{-1} , vs. temperature, T , measured along the [100] direction for the solid solution $\text{Pu}_{0.6}\text{Y}_{0.4}\text{Sb}$

[99VLMR]. $\Theta_p = 46.2$ K, $p_{\text{eff}} = 1.05 \mu_B/\text{Pu}$ at. (c) Magnetic moment p (in $\mu_B/\text{F.U.}$) vs. applied magnetic field, H , measured along three main crystallographic directions at 4.2 K [99VLMR]. Note that no spontaneous moment exists. The curves result from the splitting of the CEF levels under the applied field. Clearly, the easy axis is now the [111] direction. This behaviour makes close similarity to that in CeSb.

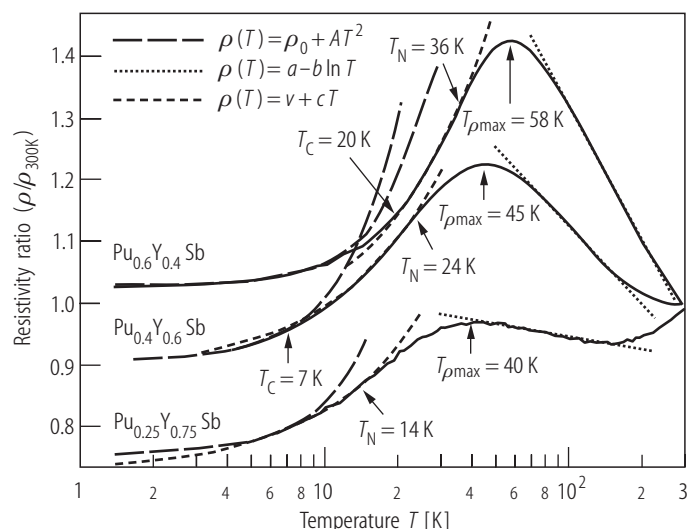


Fig. V.154. (Pu,Y)Sb s.c. Electrical resistivity ratio, $\rho(T)/\rho(300\text{ K})$, vs. $\log T$ for three solid solutions $\text{Pu}_{1-x}\text{Y}_x\text{Sb}$, where $x = 0.4, 0.6$ and 0.75 [98RWRB]. At low temperature, between 15 and 50 K, the data were fitted to a $\rho_0 + AT^2$ law (long-dashed lines), where A is proportional to x . All the curves are passing through a maximum at temperatures 58, 45 and 40 K, respectively (vertical arrows). For the two first compositions, the Curie and Néel temperatures are marked by arrows and by analogy with pure PuSb were determined by the lower and upper limit of the linear variation (short-dashed lines). The sample with $x = 0.75$ shows only one transition temperature. The transition temperatures, indicated in the figure, are as those derived from magnetic susceptibility measurements [97VMR]. Over the maximum in $\rho(T)$, which is attributed to CEF effects, the logarithmic decrease in this dependence indicates a Kondo-type behaviour.

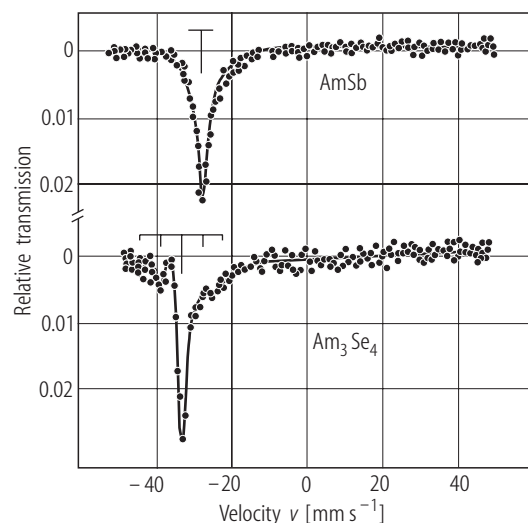


Fig. V.155. AmSb, Am_3Se_4 . Mössbauer resonance spectra at 4.2 K as a source for the 59.6 keV NGR resonance in ^{237}Np [71DLKS]. NGR isomer shift shows that the Am ion in AmSb is in a non-magnetic trivalent state. χ_m is independent of temperature, being $1250(100) \cdot 10^{-6} \text{ emu/mol}$ at temperatures between $4.2 < T < 320 \text{ K}$. Based on $\text{Am}^{3+} (5f^6)$ ion, a CF calculation performed in IC scheme, with parameters $A_4 \langle r^4 \rangle = 2365 \text{ cm}^{-1}$ and $A_6 \langle r^6 \rangle = 500 \text{ cm}^{-1}$, gives a value close to the experimental value of $\chi_m = 1120 \cdot 10^{-6} \text{ emu/mol}$. Calculation shows that there is a large separation of 2037 cm^{-1} between a singlet as the ground state and the first excited triplet state.

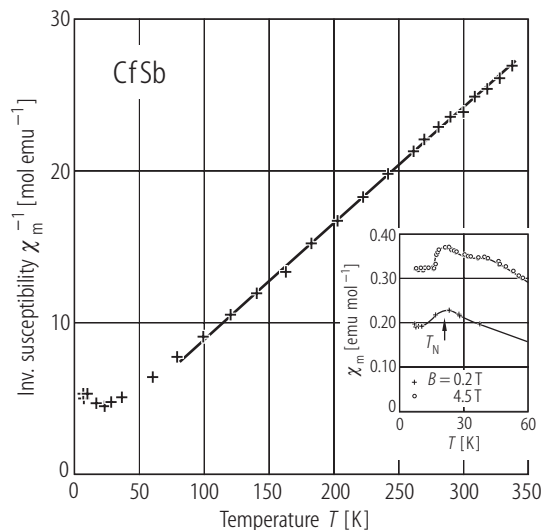


Fig. V.156. CfSb. Inverse molar magnetic susceptibility, χ_m^{-1} , vs. temperature, T , [86NMHP], [87HN]. $T_N = 25(5) \text{ K}$, $p_{\text{eff}} = 10.3(2) \mu_B$ and $\Theta_p = -18.2 \text{ K}$. The effective moment is close to values of $10.2 \mu_B$ and $10.3 \mu_B$ for the $f^9(\text{Cf}^{3+})$ and $f^{10}(\text{Cf}^{2+})$ configurations, respectively, based on an intermediate coupling model. The inset shows χ_m vs. T at low temperatures measured at two different magnetic fields 0.2 T (crosses) and 4.5 T (open circles).